INTERNATIONAL JOURNAL OF SOLIDS AND STRUCTURES
2019, vol. 164, 168190
https://doi.org/10.1016/J.IJSOLSTR.2018.12.032

A new framework for the formulation and validation of cohesive mixed-mode delamination models

Federica Confalonieri[a,*], Umberto Perego[b]

[a] *University of Pavia, Department of Civil Engineering and Architecture, via Ferrata 3, 27100 Pavia, Italy*
[b] *Politecnico di Milano, Department of Civil and Environmental Engineering, piazza L. da Vinci 32, 20133 Milano, Italy*

Abstract

A new framework for the formulation and validation of interface cohesive models for mixed mode I-mode II delamination with variable mode-ratio is presented. The approach is based on a free energy decomposition driven by the identification of three main damage modes in the tensile plane of normal and shear tractions and leads to models thermodynamically consistent for any loading path. A model with a bilinear traction-separation law is developed in detail within the proposed framework. The considered model requires a limited number of easily identifiable parameters: the traction-separation laws in the pure modes with their fracture energies, plus two phenomenological parameters, responsible for the mixed-mode interaction between the mode I and mode II failure modes, that directly affect the shape of the damage activation locus, namely an exponent and a constitutive parameter, the latter geometrically defined as an internal angle. The overall fracture energy at any mode-ratio is an outcome of the model, without the need to introduce any empirical laws, and depends on the actually followed loading path. A rigorous validation protocol, including consistency, accuracy and evolutionary tests is proposed and used for the model validation. Several tests proposed in the literature, along different proportional and non-proportional loading paths, with application to the simulation of pure and mixed-mode tests for a variety of composite materials, are considered obtaining in all cases, consistent and accurate results.

Keywords: delamination, mixed-mode, cohesive, isotropic damage, free energy decomposition, non-proportional loading.

1. Introduction

Delamination and debonding are typical failure modes for composite laminates and adhesive junctions, respectively. While in mixed-mode propagation through an isotropic brittle solid a crack tends

* Corresponding author
Email addresses: federica.confalonieri@unipv.it (Federica Confalonieri), umberto.perego@polimi.it (Umberto Perego)

naturally to realign along a mode I direction, in the case of layered composites or adhesive junctions, the delamination front is usually forced to propagate along the low toughness interface, so that mixed-mode is the most frequent loading condition. The accurate simulation of these failure processes requires therefore models capable to reproduce the interaction between different failure modes, for varying mode-ratios and along arbitrary loading paths.

A notable feature of mixed-mode delamination is that, according to experimental evidences, the energy dissipated per unit of delaminated surface, the fracture energy, depends on the active fracture mode and may be significantly different in mode I and mode II (see e.g., Hutchinson and Suo, 1991; Benzeggagh and Kenane, 1996). A fundamental understanding about the variation of the delamination failure mechanism with the mode-ratio can be gained by looking at fractographic images of the delaminated surfaces (see, e.g., Greenhalgh, 2009). Planar fracture geometries are rarely observed, with mode II loading components promoting out-of-plane features, such as cusps and hackles, with specific geometric shapes that evolve from pure mode I to pure mode II loading conditions. The higher irregularity and complexity of the fracture surface, with a resulting greater effective area, accounts for the increasing fracture energy in passing from mode I to mode II delamination (see e.g. Lee, 1997, for an attempt to establish an analytical relation between the fracture energy G_{IIc} in mode II and the corresponding G_{Ic} in mode I). The extent of this effect depends on the particular type of composite material. It is, for instance, particularly evident in thermoset fiber-reinforced matrix composites, while it is much less evident in composites with a tougher matrix, such as thermoplastic fiber-reinforced composites, where usually $G_{IIc} \approx G_{Ic}$.

A comprehensive survey of toughness variations with the mode-ratio for a number of fiber reinforced polymeric matrix composites has been reported in Davidson and Zhao (2007), where it can be appreciated the wide range of different responses exhibited by different types of composites, though belonging to the same macro-family of fiber reinforced laminates. From these data, it appears that the challenge is to formulate a delamination model, general enough to be able to accurately reproduce all this variety of different behaviors, with potentially large variations of the fracture energy with the mode-ratio, along arbitrary loading paths, by just varying a limited number of material parameters, easily identifiable by means of a well defined set of experimental tests.

Even though new approaches are now emerging (see e.g., Yuan and Fish, 2016; Simon et al., 2017), cohesive models still represent one of the most reliable and effective tools for the simulation of delamination. The literature on cohesive delamination models is particularly abundant and a comprehensive review is outside the scope of the present paper. Cohesive models may differ, for instance, for the shape of the traction-separation law (bilinear, piecewise linear, polynomial, exponential, etc.), for the way the strength degradation is treated (damage, damage combined with plasticity, softening plasticity, etc.), for the way the interaction between the failure modes is treated. A first, coarse classification may distinguish

between mixed-mode cohesive models derived from a potential function and non-potential based damage models or damage models based on a stored energy potential.

Models of the first kind postulate the existence of a potential function of the opening displacements and the tractions are obtained as derivatives of the potential with respect to the displacements. These models are intrinsically path-independent and are attractive in view of their simplicity and the fact that they are usually based on the definition of a limited number of parameters (see e.g., Park and Paulino, 2013, for a review).

Non-potential based cohesive interface models and models based on a stored energy potential are dissipative, path-dependent models, with strength and stiffness degradation driven by the growth of a damage variable. Some of these models are thermodynamically consistent, formulated within the framework of continuum damage mechanics, such as the early model by Allix and Corigliano (1996) (see also Costanzo and Allen, 1995; Mosler and Scheider, 2011, for a discussion on the formulation of thermodynamically consistent cohesive models). Other models have been developed on a more heuristic basis, such as the model by Camanho et al. (2003), with its improved version in Turon et al. (2006) to account for variable mode-ratio. In all cases, cohesive damage models require a damage activation criterion, a failure criterion and a damage evolution law. In addition, many mixed-mode models are based on the definition of equivalent tractions and displacement pairs (Ortiz and Pandolfi, 1999; Alfano and Crisfield, 2001; Camanho et al., 2003; Valoroso and Champaney, 2006; Högberg, 2006; Nguyen and Waas, 2016), to identify the proper fracture energy to be associated to a given mode-ratio. However, fixed mode-ratio (also termed radial or proportional loading) is hardly achievable in practical situations. Variable mode-ratio has been shown to be the dominant loading condition at interface material points belonging to the near-tip process zone even in the case of nominally pure-mode tests (see e.g. de Moura et al., 2016). Models explicitly addressing the issue of variable mode-ratio are for instance those by Jiang et al. (2007) and de Moura et al. (2016).

One of the main difficulties with the modeling of mixed-mode delamination is due to the difference between fracture energies in pure mode I and II, caused by the different failure mechanisms associated to the pure modes. Del Piero and Raous (2010) proposed a rigorous, thermodynamically consistent mixed-mode cohesive damage model for adhesive interfaces, based on a particular assumed form of a dissipation potential, but unable to incorporate different fracture energies in the pure modes. To overcome the problem, Parrinello et al. (2016) proposed a thermodynamically consistent model with a damage activation function containing the strain energy release rate per unit damage growth and an additional energy term, directly depending on the interface opening and sliding. The resulting model leads to different fracture energies in pure modes I and II, though there is no physical interpretation for the additional energy term. Other examples of thermodynamically consistent delamination models allowing

for different fracture energies in mode I and II have been proposed, e.g., in Allix and Corigliano (1996); Mosler and Scheider (2011); Guiamatsia and Nguyen (2014); Leuschner et al. (2015).

Several authors (see, e.g., Evans and Hutchinson, 1989; Lee, 1997) have proposed micromechanical models trying to provide physical motivations for the higher fracture energy in mode II delamination, by considering particular geometries of the fracture surfaces at the microscale. Adopting a similar approach, Serpieri et al. (2015) proposed an extension of the thermodynamically based damage model of Del Piero and Raous (2010) that, starting from the definition of a representative interface element, allowed to overcome the limitation of equal fracture energies in the pure modes. The idea was to introduce a non-planar geometry at the microscale, characterized by an angle, reflecting the geometric complexity of the fracture surface and playing the role of a constitutive parameter, so as to allow for a different dissipation for different mode-ratios. The angle defines at the microscale the inclination of microplanes on which frictional sliding may occur, thus providing the required additional dissipation in mixed-mode. The resulting macroscopic model provides an interaction between tensile-normal and shear tractions similar to the one accounted for in many damage-plasticity cohesive models proposed for the modeling of decohesion and crack propagation in concrete and other frictional materials (see e.g. Lofti and Shing, 1994; Carol et al., 1997; Cocchetti et al., 2002; Ottosen and Ristinmaa, 2013). In all these models, the activation of damage depends on an activation surface defined on the tensile side of the normal-shear tractions plane, whose geometry is defined by an angle, usually referred to as the angle of internal friction. Even though there is in general no physical evidence of the development of frictional mechanisms leading to the complex geometric patterns characterizing the mixed-mode delamination surfaces (Greenhalgh, 2009), in many cases the failure locus in the tensile tractions space can be well approximated by considering an internal angle as a constitutive parameter, playing a geometric role similar to the angle of internal friction used in the above mentioned models.

Based on these considerations, a new, thermodynamically consistent framework is proposed for the formulation of cohesive interface models suitable for the simulation of delamination under mixed mode I-mode II loading conditions. Even though only mode I-mode II mixed-mode interaction is considered, this does not limit the practical applicability of the model, since experimental evidences show that even when mode III loading is attempted, the delamination front will migrate, leading to mode II delamination in a direction parallel to the resultant of the shear force, independent of the initial direction of the defect front (Greenhalgh, 2009, sect. 4.7.1). A preliminary, synthetic version of the approach has been presented in Confalonieri and Perego (2017). A complete, detailed formulation is presented here, together with a new rigorous protocol to validate the accuracy and effectiveness of cohesive delamination models.

While in most existing models a free energy decomposition in terms of normal and shear components is considered (see, e.g., Allix and Corigliano, 1996; Mosler and Scheider, 2011), in the proposed frame-

work a new type of decomposition, driven by the identification of three damage modes is proposed. This new decomposition allows for a rational and straightforward definition of the damage activation locus, better reflecting the experimental evidences and leading to a more accurate prediction of the fracture energy variation with the mode-ratio. An internal variable, evolving with damage, is associated to each damage mode but, as in many other cohesive interface models for mixed-mode delamination (see, e.g., Alfano and Crisfield, 2001; Camanho et al., 2003; Högberg, 2006; Pinho et al., 2006; Turon et al., 2006; Valoroso and Champaney, 2006; Jiang et al., 2007; Del Piero and Raous, 2010; Guiamatsia and Nguyen, 2014; Serpieri et al., 2015; de Moura et al., 2016; Parrinello et al., 2016), the interface degradation is described by a single damage variable.

Models defined within this framework require the definition of only few parameters: the usual parameters defining the traction-separation laws in the pure modes and two additional parameters, as recommended in Reeder (1992) and in Davidson and Zhao (2007), governing the mixed-mode interaction, namely an angle defining the mixed-mode damage mechanisms and the exponent of the activation function. The angle is a phenomenological parameter reflecting macroscopically observable features of the interface behavior, but not directly related to a specific failure mechanism at the microscale. The angle is directly derivable from the shape of the envelope of peak tractions in the tensile plane, if available.

Another important feature is that, in contrast to the majority of the currently available models making use of empirical relations, such as the Power-Law (Reeder, 1992) or the B-K law (Benzeggagh and Kenane, 1996), to define a failure locus able to interpolate the toughness variation over the full mixed-mode range, in the proposed framework the failure locus is not defined a-priori, but it is the result of the interaction between modes and depends on the complete history of loading. As a consequence, the definition of equivalent opening displacements and tractions is not required and the framework is particularly suited for the simulation of complex, non-proportional loading paths. Furthermore, the proposed framework is general and, in principle, it could incorporate any form of traction-separation law, not necessarily of the same type in mode I and in mode II, adding flexibility in reproducing the mixed-mode behavior of specific types of interfaces, as, e.g., in the case of fiber-bridging. In the present work, a model based on bilinear traction-separation law for both mode I and II is developed in detail under the assumption of small opening displacements. This facilitates the presentation of the model, allowing for easier analytical derivations and for a more straightforward comparison with the performances of other existing models.

The model is intended to describe delamination processes taking place with small opening displacements. As a consequence of this, resistance mechanisms such as fiber-bridging (see, e.g., the recent contributions in Li et al., 2018; Gong et al., 2018), typically developing at the cost of large openings, are not considered, though an extension of the model to large opening displacements including fiber-bridging is currently in progress. Furthermore, the model is restricted to the case of tensile-shear traction states

and does not explicitly account for frictional effects. Shear delamination under compressive normal tractions has been considered by several authors with a number of different approaches (see, e.g., Raous et al., 1999; Alfano and Sacco, 2006; Del Piero and Raous, 2010; Guiamatsia and Nguyen, 2014; Spring and Paulino, 2015) and the proposed model could also be extended to include the case of compressive normal tractions with friction. This aspect will also be considered in a future work. The effect of friction under tensile normal tractions with small openings has been considered e.g. in Serpieri et al. (2015), with a micromechanically based damage model.

A rigorous validation protocol, consisting of three different types of tests is also proposed: consistency tests, to validate the capability of the model to account for non-proportional loading paths; accuracy tests, to validate the capability of the model to predict the fracture energy evolution with the mode-ratio for a wide range of different interfaces, exhibiting very different properties; evolutionary tests, to validate the capability of the model to accurately reproduce the history of the interface response for a number of different mode-ratios. This exhaustive and rigorous validation procedure, which to our knowledge has not been adopted before for the presentation of new interface cohesive models, has confirmed the flexibility and accuracy of the developed model for a large number of different applications.

In the case of a proportional loading path, i.e. a path where the ratio between the normal and the sliding displacements remains constant (radial path), the bilinear model allows to obtain almost analytical expressions for the response. In the more general case of non-proportional loading paths, the situation is significantly more complex: analytical approaches are not possible and several models have been shown to exhibit inconsistent results. Dimitri et al. (2015) have proposed a number of validation tests to assess the performances of different mixed-mode cohesive models under non-trivial loading conditions. Other consistency tests have been proposed in Spring et al. (2016) and Gilormini and Diani (2017). The proposed model has been validated by application to all these benchmark tests, passing them in all cases. In addition, the model has been used to predict the failure envelope in terms of fracture energy for varying mode-ratio for a number of different composite materials (Reeder, 1992; Adeyemi et al., 1999; Krueger, 2012), obtaining in all cases accurate results. Finally, the model has been implemented in a VUEL user element for the finite element code Abaqus Explicit and has been used for simulation of the three experimental tests, a double cantilever beam (DCB) test, a mixed-mode bending (MMB) test and a four-points-bend end-notched flexure (4ENF) test, presented in Pinho (2005); Pinho et al. (2006), obtaining also in this case accurate results.

2. Cohesive model

2.1. Cohesive interface

Let Γ denote a cohesive zero-thickness interface separating two adjacent material layers. Let Γ^+ and Γ^- denote the two sides of the interface after separation. Let $\boldsymbol{\delta}$ denote the vector of the small relative displacement between two initially coincident points, belonging to the two displaced sides, and let $\mathbf{t}$ be the vector of the tractions exchanged between the two sides at the same point. It is assumed that the interface exhibits an initial elastic response, with the same stiffness K in all directions, so that

$$\mathbf{t} = K\boldsymbol{\delta} \tag{1}$$

for sufficiently small $\boldsymbol{\delta}$. On physical grounds, this stiffness can be seen as originating from the interface free energy, accounting for mechanically reversible transformations, such as bond or fibril stretching, depending on the specific material considered (Costanzo and Allen, 1995). In practice, in view of the extremely small physical thickness of the interface, a very high value of the stiffness parameter is adopted, making it feasible for usage as a penalization of interpenetration under compressive stresses. The interpretation of K as a penalty stiffness justifies the use of the same parameter in normal and shear directions, as normally adopted in many works (see, e.g., Camanho et al., 2003; Pinho et al., 2006; Turon et al., 2006; Hu et al., 2008; de Moura et al., 2016). The numerical applications will show that this choice does not affect the accuracy of the results.

Tractions $\mathbf{t}$ depend on the opening displacement $\boldsymbol{\delta}$ through the traction-separation law. A typical one-dimensional traction-separation curve is shown in Figure 1, where t_0 and δ_0 denote the tractions and opening displacements at the elastic limit, respectively, t_{max} is the peak traction and δ_{cr} is the critical opening displacement, beyond which delamination starts and no more tractions are transmitted between the two separating sides.

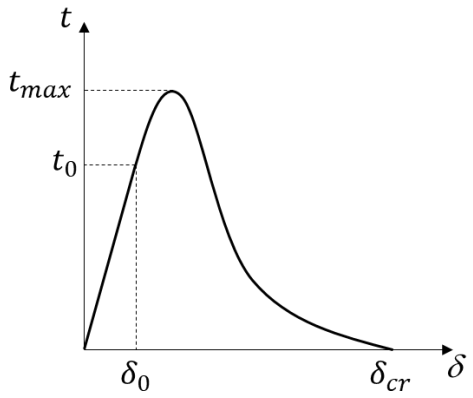

Figure 1: One-dimensional traction-separation law.

In a more general 3D case, one has

$$\mathbf{t} = \begin{Bmatrix} t^n \\ t^{s1} \\ t^{s2} \end{Bmatrix}, \quad \boldsymbol{\delta} = \begin{Bmatrix} \delta^n \\ \delta^{s1} \\ \delta^{s2} \end{Bmatrix} \tag{2}$$

where t^n and δ^n denote the components of tractions and openings normal to the initial interface Γ, while t^{s1}, t^{s2}, δ^{s1} and δ^{s2} are the corresponding shear and sliding components in the local orthogonal reference frame. Only small displacements are assumed in the present work, so that the interface local reference frame is uniquely defined by the initial interface configuration.

Since only mixed mode I-II delamination is considered, isotropic properties in the interface tangent plane (transverse isotropy) are assumed, an assumption acceptable, e.g., for many fiber or particle reinforced composites, so that $t_0^{s1} = t_0^{s2} = t_0^{II}$ and $\delta_0^{s1} = \delta_0^{s2} = \delta_0^{II}$, where t_0^{II} and δ_0^{II} are the limit elastic traction and sliding in pure mode II. This allows to reformulate, without loss of generality, the 3D problem as a 2D problem in terms of the normal components t^n, δ^n and the resultant shear traction $t^s = \sqrt{(t^{s1})^2 + (t^{s2})^2}$ and sliding displacement $\delta^s = \sqrt{(\delta^{s1})^2 + (\delta^{s2})^2}$, defined in the current sliding direction.

Non-dimensional tractions and separations are obtained by normalizing with respect to the threshold values t_0^I, t_0^{II}, δ_0^I in the pure modes and δ_0^{II}. One has:

$$\bar{\mathbf{t}} = \begin{Bmatrix} \dfrac{t^n}{t_0^I} \\ \dfrac{t^s}{t_0^{II}} \end{Bmatrix} = \begin{Bmatrix} \bar{t}^n \\ \bar{t}^s \end{Bmatrix}, \quad \bar{\boldsymbol{\delta}} = \begin{Bmatrix} \dfrac{\delta^n}{\delta_0^I} \\ \dfrac{\delta^s}{\delta_0^{II}} \end{Bmatrix} = \begin{Bmatrix} \bar{\delta}^n \\ \bar{\delta}^s \end{Bmatrix} \tag{3}$$

and hence, since $t^n = K\delta^n$, $t_0^I = K\delta_0^I$ and $t^s = K\delta^s$, $t_0^{II} = K\delta_0^{II}$, one has $\bar{\mathbf{t}} = \bar{\boldsymbol{\delta}}$.

2.2. Free energy density and state equations

The cohesive model is based on the definition of the free energy potential Ψ per unit surface:

$$\Psi = \frac{1}{2} K \left(\langle \delta^n \rangle_-\right)^2 + \frac{1}{2} (1-d) K \left(\langle \delta^n \rangle_+\right)^2 + \frac{1}{2} (1-d) K (\delta^s)^2 \tag{4}$$

where d is an internal variable accounting for interface damage. The Macauley brackets $\langle\ \rangle$ are introduced to distinguish between the negative and the positive part of the normal opening displacement, so that the unilateral effect is accounted for and interpenetration upon interface closure is prevented. According to a classical procedure (see, e.g., Lemaitre and Chaboche, 1994), imposing that the Clausius-Duhem inequality is satisfied for any arbitrary processes $\dot{\delta}^n$, $\dot{\delta}^s$ under isothermal conditions, through the state equations one obtains the expressions of the thermodynamic forces conjugate to δ^n, δ^s and to the internal

variable d, which are identified to be the tractions t^n, t^s and the strain energy release rate per unit damage growth Y:

$$t^n = \frac{\partial \Psi}{\partial \delta^n} = K\langle\delta^n\rangle_- + (1-d)\,K\langle\delta^n\rangle_+, \quad t^s = \frac{\partial \Psi}{\partial \delta^s} = (1-d)\,K\delta^s, \tag{5}$$

$$Y = \frac{1}{2}K\left(\langle\delta^n\rangle_+\right)^2 + \frac{1}{2}K\left(\delta^s\right)^2 \tag{6}$$

In view of the assumed isotropy, the relation between non-dimensional tractions and opening displacements in the damage range is simply given by

$$\bar{t}^n = (1-d)\,\bar{\delta}^n, \quad \bar{t}^s = (1-d)\,\bar{\delta}^s \tag{7}$$

where $\bar{\delta}^s$ and $\bar{t}^s$ have been defined in (3). According to equation (6), the strain energy release rate per unit damage growth turns out to be decomposed into the contributions Y^n and Y^s coming from the normal (mode I) and sliding (mode II) openings

$$Y = Y^n + Y^s, \quad Y^n = \frac{1}{2}K\left(\langle\delta^n\rangle_+\right)^2 = \frac{1}{2}t_0^I\delta_0^I\left(\langle\bar{\delta}^n\rangle_+\right)^2, \quad Y^s = \frac{1}{2}K\left(\delta^s\right)^2 = \frac{1}{2}t_0^{II}\delta_0^{II}\left(\bar{\delta}^s\right)^2 \tag{8}$$

Following a standard interpretation, Y can be viewed as the driving force promoting the development of damage and Y^n and Y^s are the quantities used in the damage activation condition to assess whether the conditions for damage growth are satisfied (see, e.g., Allix and Corigliano, 1996; Alfano and Crisfield, 2001; Valoroso and Champaney, 2006; Mosler and Scheider, 2011).

In the subsequent developments, for the sake of simplicity, only the tensile case (i.e., $\langle\delta^n\rangle_- = 0$) will be considered, interpenetration under compressive normal tractions being penalized by the high assumed stiffness K. This assumption implies that frictional effects under compressive normal tractions are not taken into account in the present model. The extension of the model to include frictional dissipation mechanisms under compression is however possible and will be discussed in a forthcoming work. In the applications, the interaction between two delaminated faces under compression will be treated as a contact problem.

2.3. Damage modes and free energy decomposition

The activation of damage in mixed-mode delamination is typically determined by the traction vector attaining an activation locus in the traction components space. The shape of the activation locus depends on the specific material considered, but in most cases it can be interpreted as the result of the combined effect of a limited number of concurrent damage modes.

The experimentally observed envelopes of the peak tractions for varying mixed-mode ratio of many

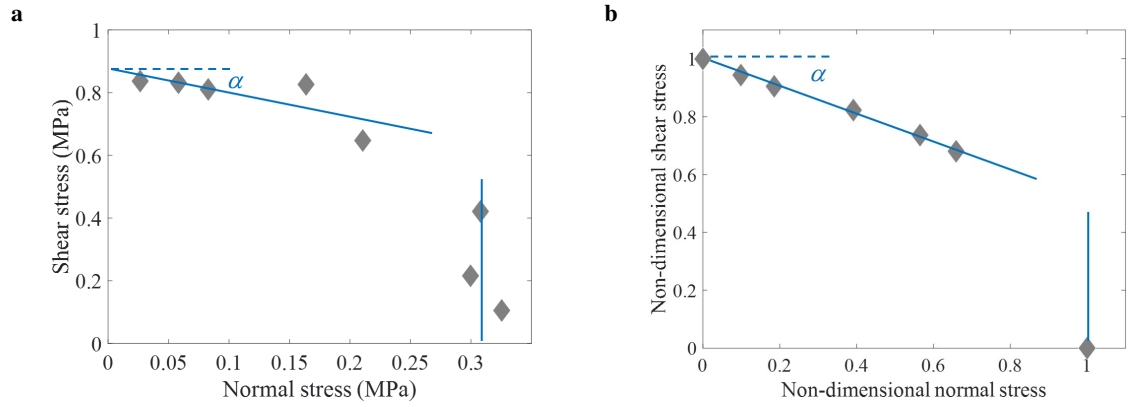

Figure 2: Experimental failure loci: a) Dunn (2000) b) Swentek and Wood (2014).

different materials (see, e.g., the envelopes in Figures 2a and b, showing experimental data taken from Dunn, 2000; Swentek and Wood, 2014, for paperboard and polymer matrix composites, respectively) suggest that the data points tend to form different groups, each one lying onto a nearly straight line. This observation allows to identify the three main damage modes shown in Figure 3, in the tensile side of the non-dimensional tractions plane (see also Cocchetti et al., 2002, for a similar definition of the elastic domain for an elastoplastic cohesive interface): a normal opening mode, associated to mode I delamination and characterized by the normal $\mathbf{n}^1$; two mixed-mode mechanisms, one for positive and one for negative shear, characterized by the normals $\mathbf{n}^2$ and $\mathbf{n}^3$, identifying two planes, inclined by angles α and $-\alpha$ with respect to the t^n axis. The angle α plays the role of a constitutive parameter. The term "damage modes" is used here in a phenomenological sense, since no attempt is made to establish a direct connection between the three damage modes and physical dissipation mechanisms at a lower scale. Rather, as it will be shown hereafter and in the next section, the three identified "damage modes" will be used to drive an unconventional decomposition of the free energy and to define in a rational way a damage activation function with three internal variables, each one attached to the corresponding "damage mode". In what follows, the term "damage mode" will be used in this broader sense.

With reference to Figure 3, where a sketchily representation of the activation locus in the 2D tractions plane is proposed, one has

$$\mathbf{n}^1 = \begin{Bmatrix} 1 \\ 0 \end{Bmatrix}, \quad \mathbf{n}^2 = \begin{Bmatrix} \sin\alpha \\ \cos\alpha \end{Bmatrix}, \quad \mathbf{n}^3 = \begin{Bmatrix} \sin\alpha \\ -\cos\alpha \end{Bmatrix} \tag{9}$$

$$\mathbf{m}^1 = a\mathbf{n}^1 = \begin{Bmatrix} a \\ 0 \end{Bmatrix}, \quad \mathbf{m}^2 = b\begin{Bmatrix} \sin\alpha \\ \cos\alpha \end{Bmatrix}, \quad \mathbf{m}^3 = b\begin{Bmatrix} \sin\alpha \\ -\cos\alpha \end{Bmatrix} \tag{10}$$

where a and b are constants defining the magnitude of the vectors $\mathbf{m}^1$ and $\mathbf{m}^2$, $\mathbf{m}^3$, respectively. These structural vectors will be used to obtain the decomposition of the free energy mentioned above.

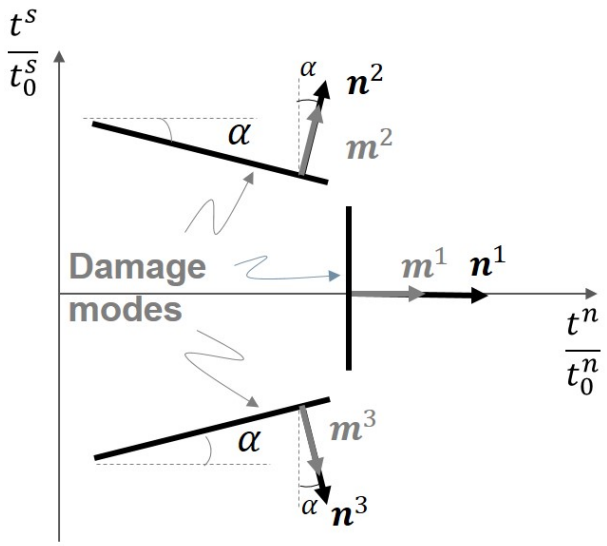

Figure 3: Main damage modes in tensile tractions plane.

From Figure 3, one can note that: due to symmetry, $\mathbf{n}^1$ must be parallel to the direction of $\bar{t}^n$; the angle α is limited by the condition $\alpha < 45°$, since for $\alpha \to 45°$ the first damage mode, defined by the normal $\mathbf{n}^1$, disappears. As it will be clarified in the next section, the consideration of both the symmetric damage modes defined by $\mathbf{n}^2$ and $\mathbf{n}^3$ is necessary to guarantee that the normal to the failure locus, resulting by application of the model, is parallel to $\bar{t}^n$ for $\bar{t}^s = 0$.

The activation of damage is assumed to depend on effective tractions obtained by projecting the traction vector onto the normal to the damage modes. The effective tractions $\mathbf{s} = \{s^1 \; s^2 \; s^3\}^T$ are used to measure the distance of the current traction vector from the activation locus:

$$\begin{aligned} s^1 &= \bar{\mathbf{t}} \cdot \mathbf{n}^1 = \bar{t}^n \\ s^2 &= \bar{\mathbf{t}} \cdot \mathbf{n}^2 = \bar{t}^n \sin\alpha + \bar{t}^s \cos\alpha \\ s^3 &= \bar{\mathbf{t}} \cdot \mathbf{n}^3 = \bar{t}^n \sin\alpha - \bar{t}^s \cos\alpha \end{aligned} \tag{11}$$

In a similar way, one can also define effective openings w^1, w^2, w^3, conjugate to the effective tractions, by projecting the interface opening displacements onto the directions defined by the three structural vectors $\mathbf{m}^1$, $\mathbf{m}^2$, $\mathbf{m}^3$ defined in (10) (Figure 3):

$$\begin{aligned} w^1 &= \bar{\boldsymbol{\delta}} \cdot \mathbf{m}^1 = a\bar{\delta}^n \\ w^2 &= \bar{\boldsymbol{\delta}} \cdot \mathbf{m}^2 = b\left[\bar{\delta}^n \sin\alpha + \bar{\delta}^s \cos\alpha\right] \\ w^3 &= \bar{\boldsymbol{\delta}} \cdot \mathbf{m}^3 = b\left[\bar{\delta}^n \sin\alpha - \bar{\delta}^s \cos\alpha\right] \end{aligned} \tag{12}$$

The constants a and b defining the magnitude of the structural vectors can be determined by enforcing

the following energy equivalence

$$\Psi = \frac{1}{2}\mathbf{t}\cdot\boldsymbol{\delta} = \frac{1}{2}\left(t_0^I\delta_0^I\,\bar{t}^n\bar{\delta}^n + t_0^{II}\delta_0^{II}\,\bar{t}^s\bar{\delta}^s\right) = \underbrace{\frac{1}{2}s^1w^1}_{\Psi^1} + \underbrace{\frac{1}{2}s^2w^2}_{\Psi^2} + \underbrace{\frac{1}{2}s^3w^3}_{\Psi^3} \tag{13}$$

obtaining

$$a = \left(t_0^I\delta_0^I - t_0^{II}\delta_0^{II}\tan^2\alpha\right), \qquad b = \frac{t_0^{II}\delta_0^{II}}{2\cos^2\alpha} \tag{14}$$

Equation (13) allows for a straightforward decomposition of the free energy driven by the identified damage modes. As a consequence, the energy released per unit damage growth is also decomposed as follows:

$$\begin{aligned} Y^1 &= -\frac{\partial\Psi^1}{\partial d} = \frac{1}{2}\left(t_0^I\delta_0^I - t_0^{II}\delta_0^{II}\tan^2\alpha\right)\left(\bar{\delta}^n\right)^2 \\ Y^2 &= -\frac{\partial\Psi^2}{\partial d} = \frac{1}{4}t_0^{II}\delta_0^{II}\left(\bar{\delta}^n\tan\alpha + \bar{\delta}^s\right)^2 \\ Y^3 &= -\frac{\partial\Psi^3}{\partial d} = \frac{1}{4}t_0^{II}\delta_0^{II}\left(\bar{\delta}^n\tan\alpha - \bar{\delta}^s\right)^2 \end{aligned} \tag{15}$$

with:

$$Y^1 + Y^2 + Y^3 = \frac{1}{2}t_0^I\delta_0^I\left(\bar{\delta}^n\right)^2 + \frac{1}{2}t_0^{II}\delta_0^{II}\left(\bar{\delta}^s\right)^2 = Y \geq 0 \quad \forall\bar{\delta}^n,\bar{\delta}^s \tag{16}$$

It should be observed that the free energy decomposition in (13) is only instrumental to the definition of the damage activation condition, as it will be shown in the next session, and cannot be attributed a thermodynamic meaning. As long as the strain energy release rate per unit damage growth $Y = Y^1 + Y^2 + Y^3$ is non-negative, the fact that Y^1 can be negative does not represent any thermodynamic fault.

Of particular interest are the expressions of the energy release rate components Y^i in the cases of pure mode I and II loading conditions, which are obtained by imposing that:

$$\delta^n \neq 0 \quad \delta^s = 0 \qquad \text{for pure mode I} \tag{17}$$

$$\delta^n = 0 \quad \delta^s \neq 0 \qquad \text{for pure mode II} \tag{18}$$

The components $Y^{1,I}$, $Y^{2,I} = Y^{3,I}$ and $Y^{1,II}$, $Y^{2,II} = Y^{3,II}$ under pure mode I and II loading conditions, respectively, are obtained by substituting (17) and (18) into (15):

$$\begin{aligned} Y^{1,I} &= \frac{1}{2}\left(t_0^I\delta_0^I - t_0^{II}\delta_0^{II}\tan^2\alpha\right)\left(\bar{\delta}^n\right)^2 \\ Y^{2,I} &= Y^{3,I} = \frac{1}{4}t_0^{II}\delta_0^{II}\tan^2\alpha\left(\bar{\delta}^n\right)^2 \end{aligned} \tag{19}$$

$$Y^{1,II} = 0$$
$$Y^{2,II} = Y^{3,II} = \frac{1}{4} t_0^{II} \delta_0^{II} \left(\bar{\delta}^s\right)^2 \tag{20}$$

It should also be noted that for $\alpha = 0$ one obtains the classical decomposition of the strain energy release rate in mode I and mode II components, with $Y^{1,I} = Y^n$, $Y^{2,I} = Y^{3,I} = 0$ and $Y^{2,II} = Y^{3,II} = 1/2Y^s$, $Y^{1,II} = 0$, where Y^n and Y^s have been defined in (8).

2.4. Damage activation condition

The purpose of the energy decomposition in (13) is to provide a rational basis for the formulation of a damage activation condition, as the one shown below, capable to reproduce envelopes of peak tractions of the type in Figure 2:

$$\varphi = \left(\frac{Y^1}{\chi_0^1 + \chi^1(d)}\right)^k + \left(\frac{Y^2}{\chi_0^2 + \chi^2(d)}\right)^k + \left(\frac{Y^3}{\chi_0^3 + \chi^3(d)}\right)^k - 1 \leq 0 \tag{21}$$

In (21), the terms $Y^i / \left(\chi_0^i + \chi^i(d)\right)$ can be interpreted as the normalized driving forces acting on each of the damage modes in Figure (3), the denominator representing the current threshold value for that mode. In (21), φ is the activation function, the exponent k is a parameter of the model and $\chi_0^i > 0$ represents the initial threshold of the i-th damage mode, while $\chi^i(d) \geq 0$, with $\chi^i(0) = 0$, is the internal variable governing the threshold evolution for increasing damage and determining the shape of the softening branch, with $\chi_0^2 = \chi_0^3$ and $\chi^2 = \chi^3$ because of the symmetry of the two shear dominated damage modes (Figure 3).

It is interesting to note that the damage activation function in (21) closely resembles the expression of the yield function of some material models based on the definition of multiple yield modes. In particular, Xia et al. (2002) presented an anisotropic elastoplastic constitutive law to model the in-plane behavior of paper and paperboard. The yield surface is constructed as in (21) by projecting the stress tensor onto six subsurfaces defined by their normal and by their initial distance from the origin. The model in Xia et al. (2002) has been further extended in Borgqvist et al. (2015), where a yield surface with twelve different plastic modes, constructed according to the same scheme, was considered to model also the out-of-plane response of paperboard.

From the expressions (19) and (20) of the Y^i, one can notice that the behavior in pure mode II in (20) is uncoupled, in the sense that a sliding displacement $\bar{\delta}^s$ produces a zero driving force $Y^{1,II}$, associated to the normal opening damage mechanism 1 in Figure 3. In contrast, in pure mode I in (19) one has $Y^{2,I} \neq 0$ and $Y^{3,I} \neq 0$. For this reason, to derive the expressions of the initial thresholds χ_0^i it is necessary to first define χ_0^2 and χ_0^3 in the pure mode II case and, then, to define χ_0^1 in the pure mode I case based on the results obtained for mode II.

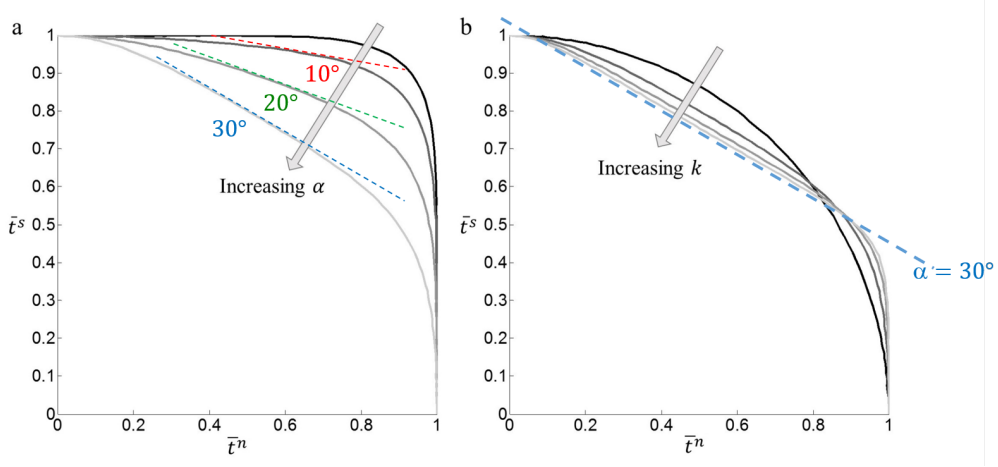

Figure 4: First activation domain: a) for increasing values of $\alpha = 0°, 10°, 20°, 30°$ and $k = 4$; b) for increasing values of $k = 2, 4, 6, 8$ and $\alpha = 30°$

In pure mode II, the initial threshold $\chi_0^2 = \chi_0^3$ can be determined by imposing that the activation criterion is fulfilled at the onset of delamination, i.e. $\varphi = 0$ for $d = 0$ and $\overline{\delta}^s = 1$, and noting that, from (20), one also has $Y^{2,II} = Y^{3,II}$:

$$\varphi = \left(\frac{Y^{2,II}\big|_{\bar{\delta}^s=1}}{\chi_0^2} \right)^k + \left(\frac{Y^{3,II}\big|_{\bar{\delta}^s=1}}{\chi_0^3} \right)^k - 1 = 2\left(\frac{Y^{2,II}\big|_{\bar{\delta}^s=1}}{\chi_0^2} \right)^k - 1 = 0 \quad \rightarrow \quad \chi_0^2 = \chi_0^3 = 2^{\frac{1}{k}} \frac{1}{4} t_0^{II} \delta_0^{II} \tag{22}$$

The initial threshold χ_0^1 can be defined in a similar way by considering pure mode I loading and noting that, from (19), one has $Y^{2,I} = Y^{3,I}$. For $\overline{\delta}^n = 1$ and $d = 0$ (i.e. for first activation), one has:

$$\varphi = \left(\frac{Y^{1,I}\big|_{\bar{\delta}^n=1}}{\chi_0^1} \right)^k + \left(\frac{Y^{2,I}\big|_{\bar{\delta}^n=1}}{\chi_0^2} \right)^k + \left(\frac{Y^{3,I}\big|_{\bar{\delta}^n=1}}{\chi_0^3} \right)^k - 1 = 0 \quad \rightarrow \quad \chi_0^1 = \frac{\frac{1}{2}\left(t_0^I \delta_0^I - t_0^{II} \delta_0^{II} \tan^2\alpha \right)}{\left[1 - (\tan^2\alpha)^k \right]^{\frac{1}{k}}} \tag{23}$$

Figure 4 shows the damage activation surface in the $\bar{t}^s - \bar{t}^n$ plane at the onset of decohesion, i.e. defining the initial elastic domain, for the case of radial loading paths, i.e. for $\bar{\delta}^s/\bar{\delta}^n = \text{const}$, (a) for increasing values of the angle α and fixed exponent $k = 4$ and (b) for increasing values of the exponent k, while maintaining a constant value of the angle $\alpha = 30°$. The plots in Figure 4 show only the symmetric part of the elastic domain, while also the part corresponding to negative shear is considered in the computations, according to equation (21). As anticipated, the consideration of the damage modes associated to both positive and negative shear guarantees that the normal to the envelops at $\bar{t}^s = 0$ is parallel to the axis $\bar{t}^n$.

Each of the points of the curves in Figure 4 has been obtained numerically by increasing the opening displacements with a prescribed ratio $\bar{\delta}^s/\bar{\delta}^n = \text{const}$ (radial loading) until the condition $\varphi = 0$ in (21) is first met (i.e. for $d = 0$). Each curve is defined by interpolating the points obtained varying the ratios $\bar{\delta}^s/\bar{\delta}^n$ with a fine step and fixed values of α and k. Figure 4 clearly shows that the chosen value of α directly reflects through (21) into the shape of the activation locus, clarifying in this way its geometrical

interpretation. Based on this consideration, α could be directly identified from experimental plots of the first damage activation locus in the tractions plane. This information is however seldom made available from the results of experimental campaigns. Therefore, an indirect identification of α from fracture energy measurements in MMB tests will be pursued in the applications.

2.5. Damage evolution and dissipation

Damage evolution is obtained in a classical way enforcing the conditions $\varphi = 0$ and $\dot{\varphi} = 0$, from which one obtains

$$\dot{d} = -\frac{\dfrac{\partial\varphi}{\partial\delta^n}\dot{\delta}^n + \dfrac{\partial\varphi}{\partial\delta^s}\dot{\delta}^s}{\dfrac{\partial\varphi}{\partial d}} = -\frac{\displaystyle\sum_{i=1}^{3}\left(\frac{\partial\varphi}{\partial Y^i}\frac{\partial Y^i}{\partial\delta^n}\right)\dot{\delta}^n + \sum_{i=1}^{3}\left(\frac{\partial\varphi}{\partial Y^i}\frac{\partial Y^i}{\partial\delta^s}\right)\dot{\delta}^s}{\displaystyle\sum_{i=1}^{3}\left(\frac{\partial\varphi}{\partial\chi^i}\frac{\partial\chi^i}{\partial d}\right)}, \quad \text{for } \varphi = 0 \tag{24}$$

The following loading-unloading conditions of Kuhn-Tucker type enforce the non-negativity and non-reversibility of damage

$$\varphi \le 0, \qquad \dot{d} \ge 0, \qquad \varphi\dot{d} = 0 \tag{25}$$

The possible combinations are therefore:

$$\text{if } \varphi = 0 \text{ and } -\frac{\displaystyle\sum_{i=1}^{3}\left(\frac{\partial\varphi}{\partial Y^i}\frac{\partial Y^i}{\partial\delta^n}\right)\dot{\delta}^n + \sum_{i=1}^{3}\left(\frac{\partial\varphi}{\partial Y^i}\frac{\partial Y^i}{\partial\delta^s}\right)\dot{\delta}^s}{\displaystyle\sum_{i=1}^{3}\left(\frac{\partial\varphi}{\partial\chi^i}\frac{\partial\chi^i}{\partial d}\right)} > 0, \text{ then } \dot{d} > 0 \tag{26}$$

$$\text{if } \varphi = 0 \text{ and } -\frac{\displaystyle\sum_{i=1}^{3}\left(\frac{\partial\varphi}{\partial Y^i}\frac{\partial Y^i}{\partial\delta^n}\right)\dot{\delta}^n + \sum_{i=1}^{3}\left(\frac{\partial\varphi}{\partial Y^i}\frac{\partial Y^i}{\partial\delta^s}\right)\dot{\delta}^s}{\displaystyle\sum_{i=1}^{3}\left(\frac{\partial\varphi}{\partial\chi^i}\frac{\partial\chi^i}{\partial d}\right)} \le 0, \text{ then } \dot{d} = 0 \tag{27}$$

$$\text{if } \varphi < 0 \text{ then } \dot{d} = 0 \tag{28}$$

The non-negative dissipation rate $\mathcal{D}$ is defined as the difference between the input power and the rate of the free energy

$$\mathcal{D} = \mathbf{t}\cdot\dot{\boldsymbol{\delta}} - \dot{\Psi} \ge 0 \quad \text{with} \quad \dot{\Psi} = \frac{\partial\Psi}{\partial\boldsymbol{\delta}}\cdot\dot{\boldsymbol{\delta}} + \frac{\partial\Psi}{\partial d}\dot{d} = \mathbf{t}\cdot\dot{\boldsymbol{\delta}} - Y\dot{d} \tag{29}$$

Hence, in view of the non-negativity (16) of Y and of the loading-unloading conditions (25), one has

$$\mathcal{D} = Y\dot{d} \ge 0 \tag{30}$$

which guarantees the thermodynamic consistency of the model. The energy dissipated up to complete decohesion in a mixed-mode loading program is given by

$$G_{cr} = G^n_{cr} + G^s_{cr}, \quad \text{with} \quad G^n_{cr} = \int_0^{\delta^n_{cr}} t^n \, d\delta^n, \quad G^s_{cr} = \int_0^{\delta^s_{cr}} t^s \, d\delta^s \tag{31}$$

where δ^n_{cr} and δ^s_{cr} are the limit values of the opening displacements, corresponding to $d = 1$, for the considered mixed-mode loading program. In pure mode I loading ($\dot{\delta}^s = 0$ throughout the loading path), one has $G^n_{cr} = G^I_{cr}$, and the energy per unit surface dissipated at a point at complete decohesion is equal to the interface fracture energy in pure mode I. Similarly, in pure mode II ($\dot{\delta}^n = 0$ throughout the loading path), one has $G^s_{cr} = G^{II}_{cr}$, G^{II}_{cr} being the fracture energy in pure mode II. Under mixed-mode loading, the dissipated energy at failure G_{cr} depends on the loading path and on the interaction between modes, which is primarily governed by the parameters α and k. This is in line with what has been advocated by several authors (see, e.g. Reeder, 1992; Davidson and Zhao, 2007), claiming that at least two parameters are required to accurately reproduce the failure locus for a wide range of materials.

It should be remarked that, in contrast to the majority of the available models, the present model does not require to specify a-priori the failure locus in terms of the fracture energy evolution with the mode-ratio, as, e.g., in the case of the B-K (Benzeggagh and Kenane, 1996) or the Power Law (Reeder, 1992) criteria. Rather, the failure locus is implicitly defined by the damage reaching its limit value 1, for which all the traction components vanish, according to (5), and complete decohesion is achieved. This allows the model to be applied without difficulty to any type of non-proportional loading path and avoids the need to define equivalent displacements and tractions in mixed-mode.

2.6. Bilinear traction-separation law

A simple bilinear law (Figure 5) will be considered for the model validation and for the simulation of mixed-mode delamination tests. The bilinear law is the most widely used, in view of its simplicity, and it is therefore convenient in order to appreciate the specific features of the proposed model in comparison to other available models. Other forms (exponential, polynomial, etc.) of the traction-separation law could be incorporated in the proposed framework at the cost of some additional analytical complications. Furthermore, it is important to note that the traction-separation laws are not required to be of the same type in mode I and in mode II. For instance, a bilinear law in mode II could be easily coupled to a trilinear law in mode I for a more accurate modeling of some types of interfaces. These types of developments will be considered in future works.

The shape of the softening branches in the pure modes is determined by the functions $\chi^i(d)$, with $\chi^2 = \chi^3$. From Figure 5, it can be seen that in both pure modes I and II the softening branch can be described by the relations

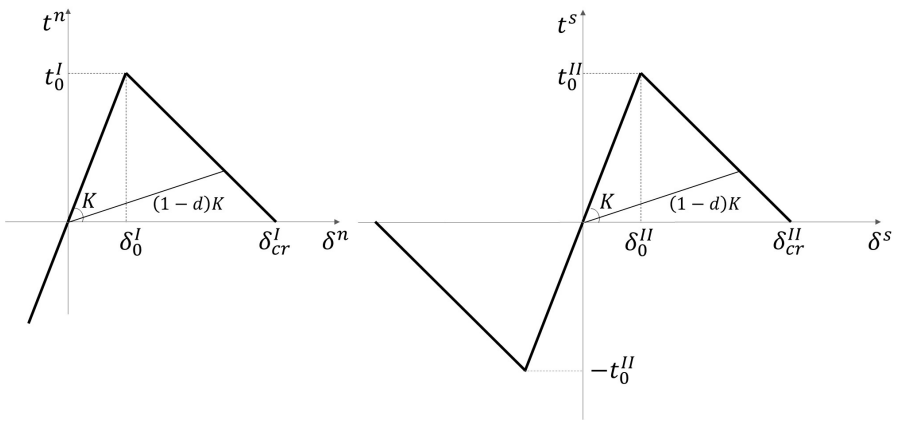

Figure 5: Bilinear traction-separation laws in pure modes I and II.

$$t^m = \frac{t_0^M}{\delta_0^M}\delta^m \qquad \text{for} \quad \delta^m \leq \delta_0^M \tag{32}$$

$$t^m = (1-d)\,\frac{t_0^M}{\delta_0^M}\delta^m = t_0^M\,\frac{\delta_{cr}^M - \delta^m}{\delta_{cr}^M - \delta_0^M} \qquad \text{for} \quad \delta^m \geq \delta_0^M \tag{33}$$

with $m = n$, $M = I$ in pure mode I and $m = s$, $M = II$ in pure mode II loading. From equation (33) it is possible to derive the relation between the damage variable d and the relative displacement δ^m for $\delta^m \geq \delta_0^M$, i.e.

$$\delta^m = \frac{\delta_{cr}^M \delta_0^M}{\delta_{cr}^M - (\delta_{cr}^M - \delta_0^M)d} \tag{34}$$

Similar to what done in Section 2.4 for the initial thresholds χ_0^i, the expression of $\chi^2 = \chi^3$ in terms of the sliding $\bar{\delta}^s$ can be found by considering a pure mode II loading case and by imposing that the activation criterion is met for $d > 0$ and $\bar{\delta}^s > 1$:

$$\varphi = \left(\frac{Y^{2,II}\big|_{\bar{\delta}^s>1}}{\chi_0^2 + \chi^2}\right)^k + \left(\frac{Y^{3,II}\big|_{\bar{\delta}^s>1}}{\chi_0^3 + \chi^2}\right)^k - 1 = 0 \quad \rightarrow \quad \chi^2 = \chi^3 = 2^{\frac{1}{k}}\frac{1}{4}t_0^{II}\delta_0^{II}\left[\left(\bar{\delta}^s\right)^2 - 1\right] \tag{35}$$

By substituting the expression (34) of $\bar{\delta}^m$ as a function of d, with $m = s$, $M = II$, into (35), one finally obtains the internal variables evolution with damage:

$$\chi^2(d) = \chi^3(d) = 2^{\frac{1}{k}}\frac{1}{4}t_0^{II}\delta_0^{II}\left[\frac{\delta_{cr}^{II}}{\delta_{cr}^{II} - \left(\delta_{cr}^{II} - \delta_0^{II}\right)d}\right]^2 - \chi_0^2 \tag{36}$$

Following the same path of reasoning for χ^1 and imposing that under mode I loading conditions the

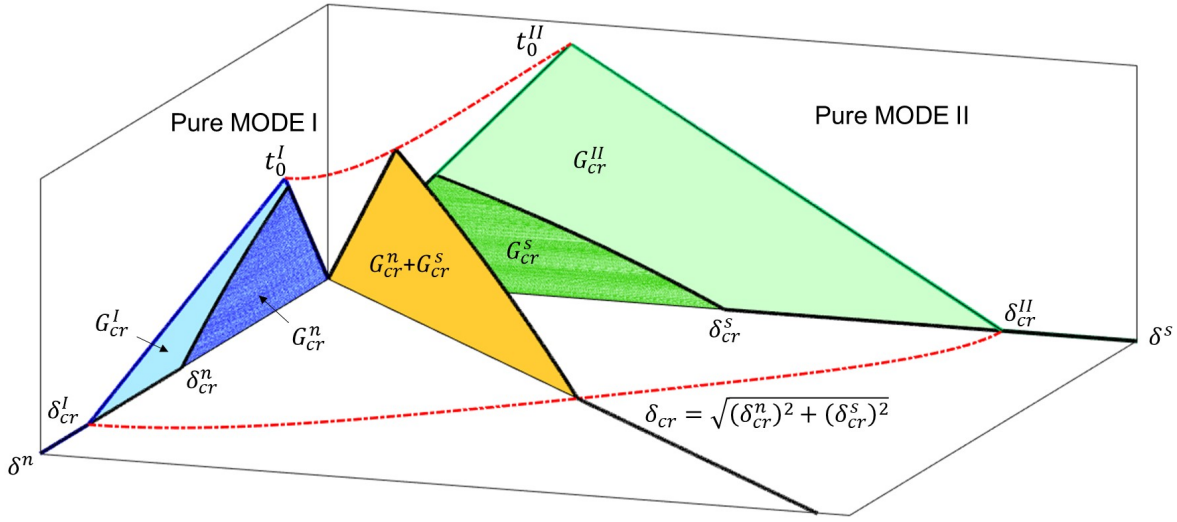

Figure 6: Mixed-mode traction-separation law for varying mode-ratio.

damage activation condition is met for a generic non-dimensional opening displacement $\bar{\delta}^n > 1$, one has:

$$\varphi = \left(\frac{Y^{1,I}\big|_{\bar{\delta}^n>1}}{\chi_0^1 + \chi^1} \right)^k + \left(\frac{Y^{2,I}\big|_{\bar{\delta}^n>1}}{\chi_0^2 + \chi^2} \right)^k + \left(\frac{Y^{3,I}\big|_{\bar{\delta}^n>1}}{\chi_0^3 + \chi^3} \right)^k - 1 = 0 \tag{37}$$

From (37), one obtains

$$\chi_0^1 + \chi^1 = \frac{Y^{1,I}}{\left[1 - 2 \left(\frac{Y^{2,I}}{\chi_0^2 + \chi^2} \right)^k \right]^{\frac{1}{k}}} \tag{38}$$

Making use of (19), (36) and of (34) with $m = 1$ and $M = I$, after some algebra one finally has:

$$\chi^1 = \frac{t_0^I \delta_0^I \left(1 - \dfrac{t_0^{II} \delta_0^{II}}{t_0^I \delta_0^I} \tan^2 \alpha \right)}{\left\{ 1 - \left[\left(\dfrac{\delta_{cr}^I}{\delta_{cr}^{II}} \dfrac{\delta_{cr}^{II} - (\delta_{cr}^{II} - \delta_0^{II})d}{\delta_{cr}^I - (\delta_{cr}^I - \delta_0^I)d} \right)^2 \tan^2 \alpha \right]^k \right\}^{\frac{1}{k}}} \frac{1}{2} \left(\frac{\delta_{cr}^I}{\delta_{cr}^I - (\delta_{cr}^I - \delta_0^I)d} \right)^2 - \chi_0^1 \tag{39}$$

At complete decohesion (i.e. for $d = 1$), the internal variables take the expressions:

$$\begin{aligned} \chi_{cr}^1 &= \frac{1}{2} \frac{\dfrac{t_0^I}{\delta_0^I} \left(1 - \dfrac{t_0^{II} \delta_0^{II}}{t_0^I \delta_0^I} \tan^2 \alpha \right) \left(\delta_{cr}^I \right)^2}{\left\{ 1 - \left[\left(\dfrac{\delta_{cr}^I}{\delta_{cr}^{II}} \dfrac{\delta_0^{II}}{\delta_0^I} \right)^2 \tan^2 \alpha \right]^k \right\}^{\frac{1}{k}}} - \chi_0^1 \\ \chi_{cr}^2 &= \chi_{cr}^3 = 2^{\frac{1}{k}} \frac{1}{4} \frac{t_0^{II}}{\delta_0^{II}} (\delta_{cr}^{II})^2 - \chi_0^2 \end{aligned} \tag{40}$$

From $(19)_1$ and (39), one has that for $d > 0$ the normalized driving force acting on the first damage

mode is given by

$$\frac{Y^1}{\chi_0^1+\chi^1}=\left\{1-\left[\left(\frac{\delta_{cr}^I}{\delta_{cr}^{II}}\frac{\delta_{cr}^{II}-(\delta_{cr}^{II}-\delta_0^{II})d}{\delta_{cr}^I-(\delta_{cr}^I-\delta_0^I)d}\right)^2\tan^2\alpha\right]^k\right\}^{\frac{1}{k}}\left\{\frac{\bar{\delta}^n}{\delta_{cr}^I}\left[\delta_{cr}^I-(\delta_{cr}^I-\delta_0^I)d\right]\right\}^2 \tag{41}$$

It can be verified that $Y^1/(\chi_0^1+\chi^1)$ is an always positive function of damage if

$$\frac{\delta_{cr}^I}{\delta_0^I}\tan\alpha<\frac{\delta_{cr}^{II}}{\delta_0^{II}} \tag{42}$$

a condition practically always satisfied in view of the higher interface toughness in mode II than in mode I. This is however a limitation of the model that should not be used if condition (42) is not satisfied.

The mixed-mode response resulting from the definition of the bilinear law is shown in Figure 6, where G_{cr}^n and G_{cr}^s have been defined in (31). The mixed-mode traction-separation curve has been obtained assigning an opening displacement monotonically growing along the straight line shown in the figure in the δ^n-δ^s plane (radial loading). It should be noted that, while in the pure modes the traction-separation laws are bilinear, in accordance with the initial assumption, the softening branch in mixed-mode is, in general, curvilinear. A notable exception is the case, which will be discussed in the next session (with details given in the Appendix), when an identical behavior is assumed in the pure modes, i.e. $t_0^I=t_0^{II}=\hat{t}_0$, $\delta_0^I=\delta_0^{II}=\hat{\delta}_0$ and $\delta_{cr}^I=\delta_{cr}^{II}=\hat{\delta}_{cr}$. The non-linearity of the softening branch in mixed-mode is a consequence of the fact that no assumptions are made a priori on the failure conditions for a given mode-ratio. As already underlined, the mixed-mode fracture energy and the critical opening displacement are the result of the model response along the prescribed loading and do not have to be prescribed in advance.

An alternative visualization of the responses of the proposed bilinear cohesive model under radial loading conditions, each characterized by a different mode-ratio, and $\alpha=30^\circ$, $k=2$, is shown in Figure 7 for the general case of different cohesive properties in the pure modes. For increasing mode-ratio, i.e. passing from pure mode I towards pure mode II, the mode I contribution decreases, i.e., the peak normal traction and the area G_{cr}^n below the traction-separation law up to complete separation become smaller and smaller. The opposite happens for the mode II contribution. As already emphasized, from the figure it can be appreciated that the softening branch, which is linear in the pure modes, becomes curvilinear in mixed-mode.

3. Consistency tests

In this section the consistency of the model is assessed by means of five different consistency tests proposed in the literature, where the model is applied to different proportional and non-proportional

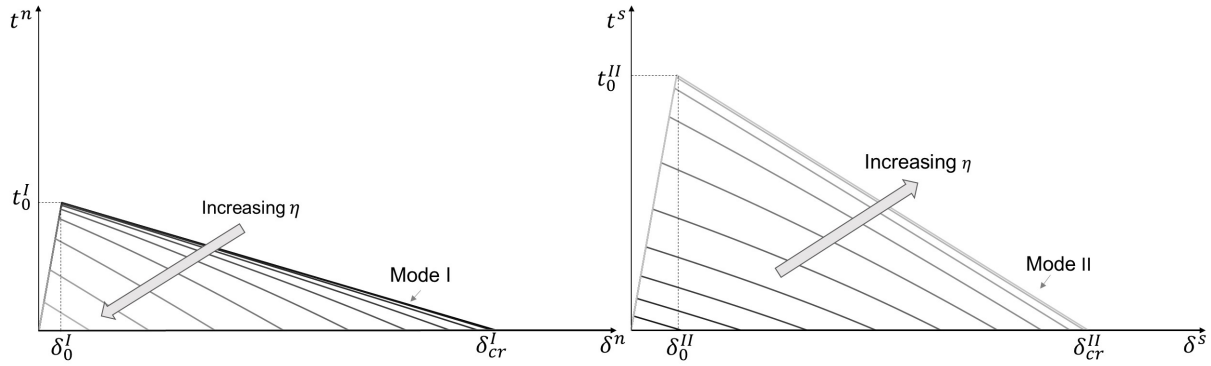

Figure 7: Mode I and Mode II components for radial loading with varying mode-ratio.

loading paths.

3.1. Radial loading with identical cohesive properties in the pure modes

The radial loading condition, i.e. with constant ratio δ^s/δ^n, is the one ideally reproduced in laboratory tests finalized to the identification of the interface properties for different mode-ratios and it is, therefore, particularly important. Let δ define a monotonically growing loading parameter such that

$$\delta^n = (1-\eta)\delta, \quad \delta^s = \eta\delta, \quad \delta = \delta^n + \delta^s \tag{43}$$

where η is a parameter related to the mode-ratio δ^s/δ^n. One has

$$\eta = \frac{\delta^s}{\delta^n + \delta^s} = \frac{\delta^s}{\delta}, \quad \frac{\delta^s}{\delta^n} = \frac{\eta}{1-\eta} \tag{44}$$

In the radial loading case, the energy dissipated for complete decohesion, i.e. the fracture energy G_{cr}, can be computed by direct integration for a given value of η. A complete derivation is proposed in Appendix A.1.

A case of particular interest consists of a cohesive model with identical behavior in the pure modes. In this case, since $t_0^I = t_0^{II} = \hat{t}_0$, $\delta_0^I = \delta_0^{II} = \hat{\delta}_0$, $\delta_{cr}^I = \delta_{cr}^{II} = \hat{\delta}_{cr}$, $G_{cr}^I = G_{cr}^{II}$, the common argument is that there is no reason why a different behavior should be obtained in mixed mode, so that the same fracture energy $G_{cr} = G_{cr}^n + G_{cr}^s = \text{const}$ should be obtained for any value of η (see, e.g. Dimitri et al., 2015).

As discussed in Appendix A.2, in the special case of identical pure modes, for the bilinear traction-separation law considered, one has that the softening branch remains linear for any mixed-mode radial path. This is in contrast with the general case of different properties in the pure modes, for which the softening branch is linear only under pure mode I or II loading conditions.

As shown in equation (A.22), in the special case of equal properties the analytical expression of the

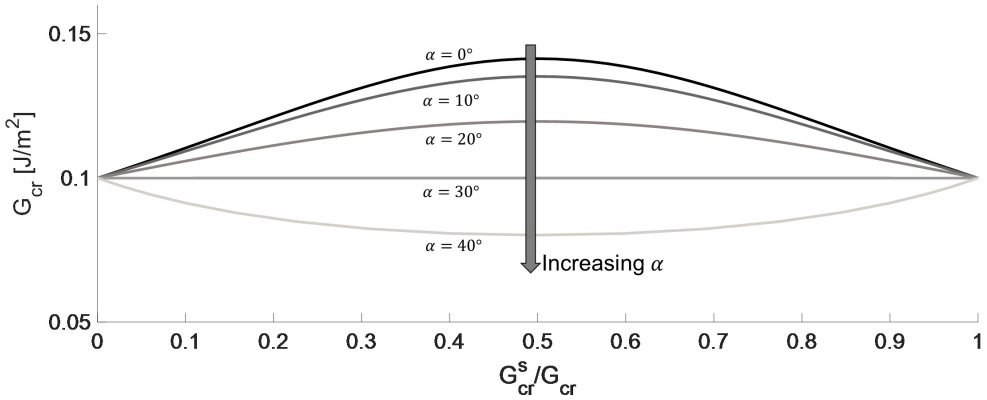

Figure 8: Fracture energy vs mode mixity for $k = 2$, $G^I_{cr} = G^{II}_{cr}$, $t^I_0 = t^{II}_0$ for increasing values of the angle α.

fracture energy in terms of the mode ratio η is given by

$$G_{cr}(\eta) = \frac{1}{2} K \hat{\delta}_0 \hat{\delta}_{cr} g^2(\eta)[(1-\eta)^2 + \eta^2] \tag{45}$$

where $g(\eta)$ has been defined in (A.14). From (45), it turns out that the fracture energy is not constant with the mode-ratio, despite the fact that identical behavior has been postulated in the pure modes. However, if the exponent $k = 2$ is assumed, in view of (A.15), G_{cr} turns out to vary symmetrically with respect to $\eta = 0.5$ and, if also $\alpha = 30°$ is assumed, in view of (A.16), the fracture energy becomes constant, independent of the mode-ratio η. For a suitable choice of parameters, i.e. $k = 2$ and $\alpha = 30°$, the model is then capable to reproduce correctly the requirement of constant fracture energy in the case of identical behavior in the pure modes. For $k = 2$, the evolution of the fracture energy G_{cr} with the mode-ratio, expressed in terms of the ratio $\gamma = G^s_{cr}/G_{cr}$ is shown in Figure 8. Increasing the internal angle α has the effect of reducing the peak value of G_{cr}, without changing its position because of symmetry. For $\alpha = 30°$, the model reproduces the case of constant fracture energy.

3.2. Non-proportional paths

Two non-proportional loading paths, combining normal and shear loading, as proposed in van den Bosch et al. (2006); Park et al. (2009); Dimitri et al. (2015), are considered in this consistency test: in the first path (Figure 9a), the interface is loaded first in the normal direction up to $\delta^n = \Delta^n_{max}$ and, then, in the sliding direction up to failure, keeping the normal opening displacement constant; conversely, in the second path (Figure 9b), the interface is subjected first to a sliding displacement increasing up to $\delta^s = \Delta^s_{max}$ and, then, to a normal opening, up to complete decohesion, while the sliding is kept fixed.

For each of the two types of path, the test is repeated considering increasing values of Δ^n_{max} and Δ^s_{max} respectively, both ranging from 0 to the value corresponding to complete decohesion. The total work of

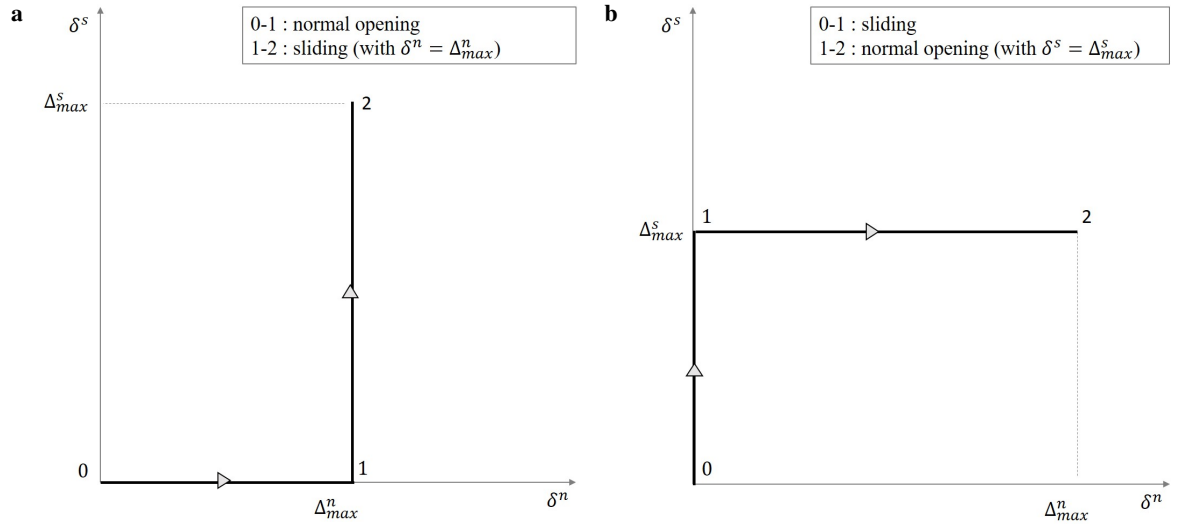

Figure 9: Non-proportional loading paths. a) Path 1, b) path 2.

t_0^I MPa	t_0^{II} MPa	G_{cr}^I $\frac{N}{mm}$	G_{cr}^{II} $\frac{N}{mm}$	K $\frac{N}{mm^3}$	α deg	k -
6	6	0.1	0.1	10,000	30	2

Table 1: Non-proportional loading paths. Adopted cohesive properties in the case of identical parameters in the pure modes.

separation, corresponding to the energy dissipated along the path and defined as:

$$W = \underbrace{\int_\Gamma t^n \, d\delta^n}_{W^n} + \underbrace{\int_\Gamma t^s \, d\delta^s}_{W^s} \tag{46}$$

being Γ the selected loading path, is computed along all the considered paths.

The test has been first carried out considering identical properties in the pure modes, as reported in Table 1: the parameters have been taken from Dimitri et al. (2015) except for the elastic stiffness, because of the fact that two distinct values for the elastic stiffnesses in pure modes have been employed in Dimitri et al. (2015). As expected, constant work of separation for all loading paths is obtained with $\alpha = 30°$ and $k = 2$, as can be seen in Figure 10a, which displays the work of separation as a function of Δ^n_{max} normalized by δ_0^I, computed for the first loading path and in Figure 10b for the second loading path, which shows the work of separation as a function of Δ^s_{max}, normalized by δ_0^{II}. The contributions

t_0^I MPa	t_0^{II} MPa	G_{cr}^I $\frac{N}{mm}$	G_{cr}^{II} $\frac{N}{mm}$	K $\frac{N}{mm^3}$	α deg	k -
6	6	0.1	0.2	10,000	30	2

Table 2: Non-proportional paths. Adopted cohesive properties in the case of different properties in pure modes.

due to W^n and W^s are represented by the dashed gray and the dot-dash gray lines, respectively, while the black solid line gives the overall work of separation W.

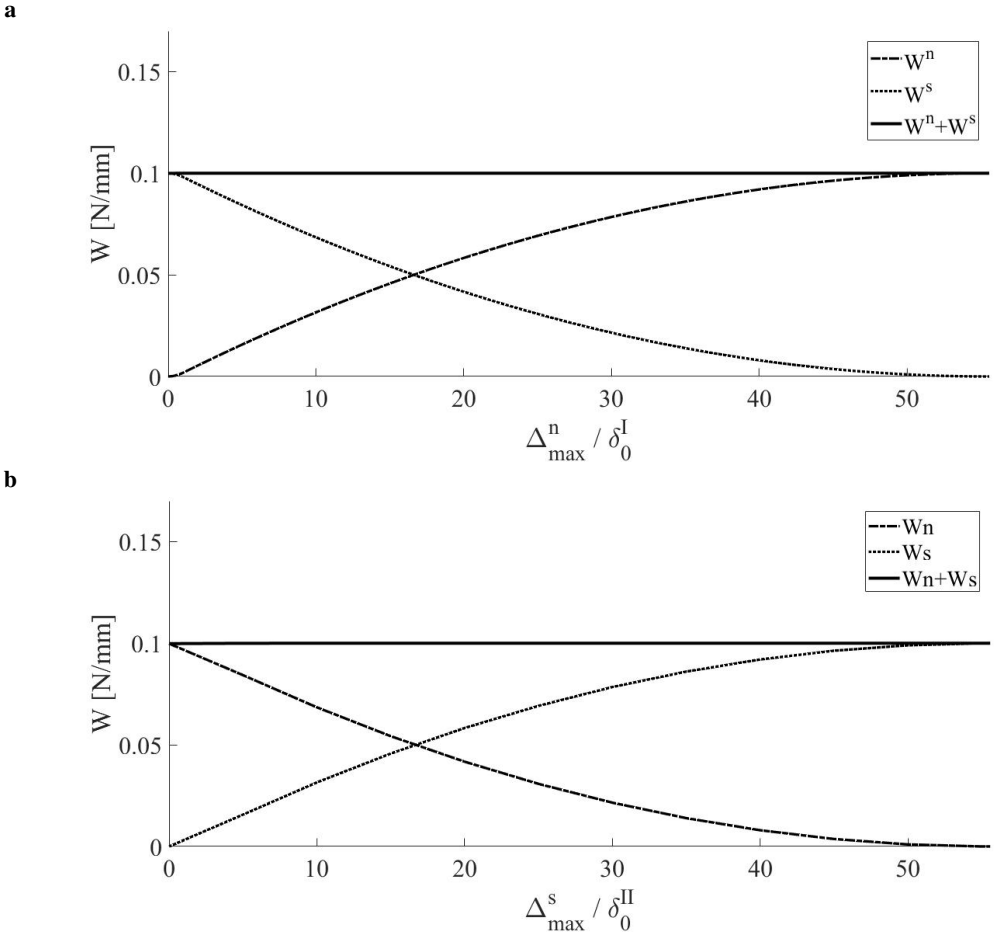

Figure 10: Non-proportional loading paths in the case of identical properties in pure modes. a) Path 1, b) path 2.

Different properties in pure mode I and II, summarized in Table 2 (also in this case, the peak stresses and the fracture energies have been taken from Dimitri et al., 2015), have been considered in Figure 11. As expected, for $\Delta^n_{max} = 0$ mm the work of separation is equal to the fracture energy G^{II}_{cr} in pure mode II, while the fracture energy G^I_{cr} in pure mode I is recovered for $\Delta^n_{max} = 55.56\delta^I_0$. A smooth transition between the two is obtained under mixed-mode conditions.

The work of separation computed for the second loading path is shown in Figure 12 as a function of Δ^s_{max} normalized by δ^{II}_0. Also in this case, the overall work of separation W varies smoothly from the value of the fracture energy in pure mode I for $\Delta^s_{max} = 0$ mm, to the one of pure mode II for $\Delta^s_{max} = 111.11\delta^{II}_0$.

Figures 13 and 14 show the total work of separation W^n along the two loading paths, computed with different values of the angle α, namely 0°, 10°, 20°, 30° and 40°, and for $k = 2$. Even though in all the cases the transition is smooth, the angle α sensibly affects the response. It can be seen that, for values of α sufficiently large, the total work of separation W remains included in the range $G^I_{cr} - G^{II}_{cr}$ for all loading

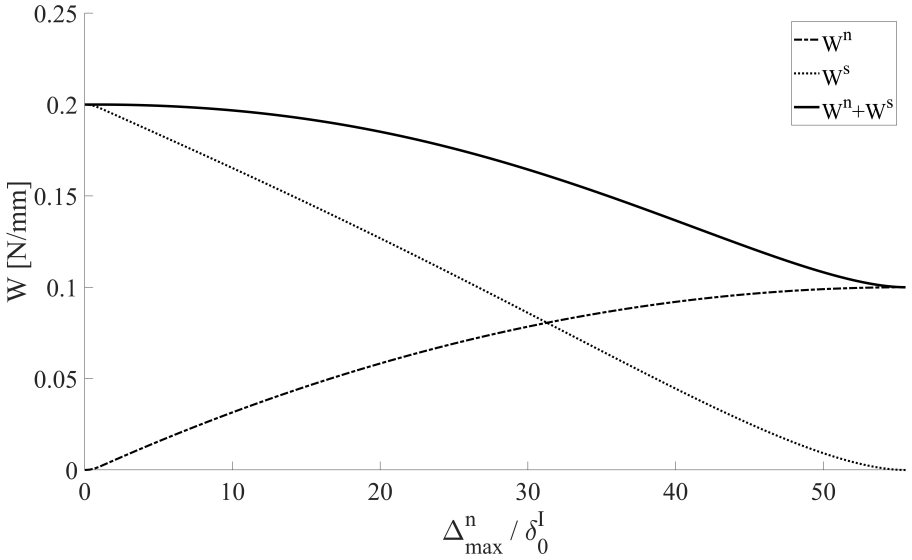

Figure 11: Non-proportional path 1. Works of separation as a function of the ratio $\Delta^n_{max}/\delta^I_0$ in the case of different properties in pure modes.

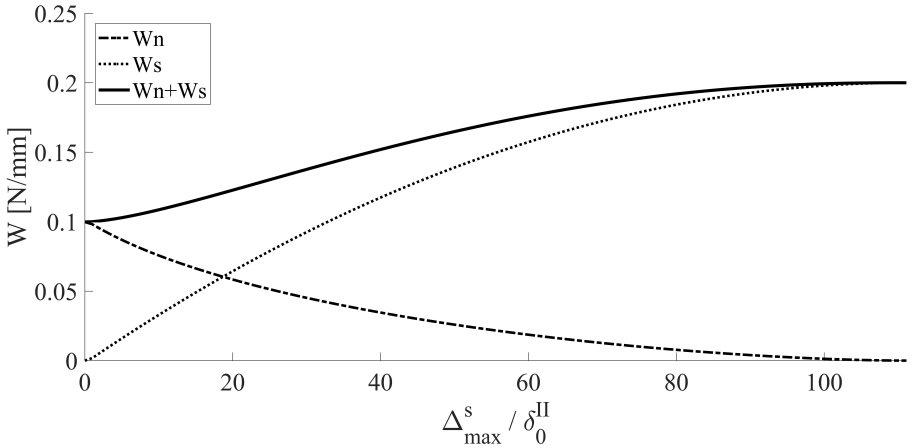

Figure 12: Non-proportional path 2. Works of separation as a function of the ratio $\Delta^s_{max}/\delta^{II}_0$ in the case of different properties in pure modes.

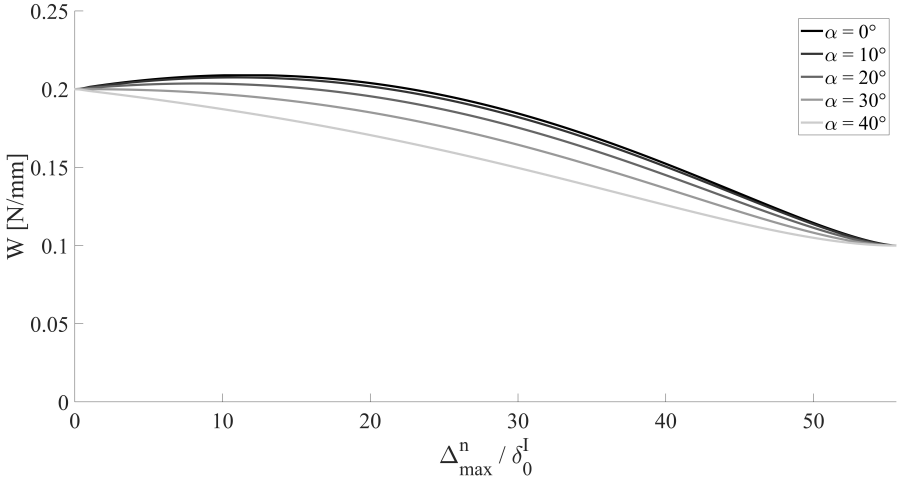

Figure 13: Non-proportional path 1. Total work of separation computed for different values of α and $k = 2$ in the case of different properties in pure modes.

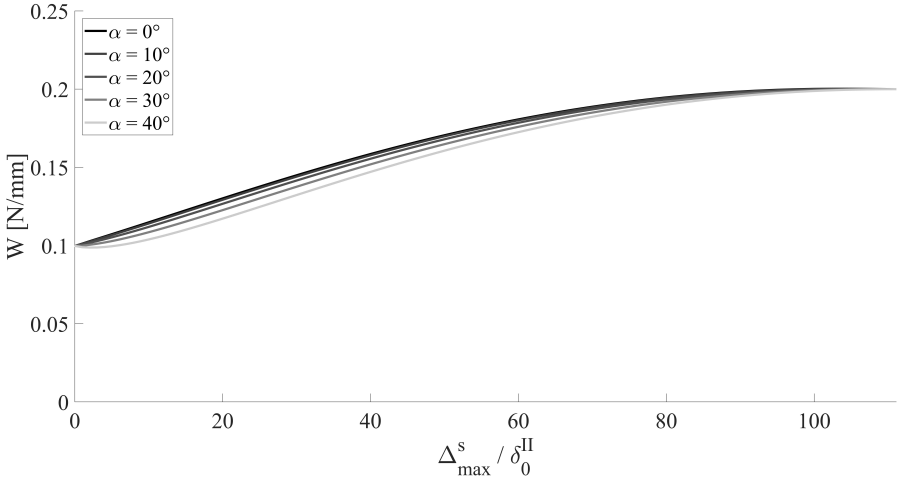

Figure 14: Non-proportional path 2. Total work of separation computed for different values of α and $k = 2$ in the case of different properties in pure modes.

paths, satisfying a condition that is considered by many authors as a desirable requisite for mixed-mode delamination models (see, e.g., Dimitri et al., 2015).

3.3. Non-proportional unloading/reloading path

A test conceptually similar to the one discussed in section 3.2, though along a different path, has been proposed in Gilormini and Diani (2017): the interface is at first loaded proportionally with $\delta^n = \delta^s$, i.e. $\eta = 0.5$, up to $\delta = 2\Delta_{max}$ in (43), then completely unloaded following the same path and, finally, reloaded in pure mode I up to complete failure, as shown in Figure 15a. The cohesive properties considered in this numerical example, reported in Table 3, are the same proposed in Gilormini and Diani (2017).

The test is performed considering an increasing value of the maximum opening displacement Δ_{max} reached at the end of the proportional path and computing the corresponding work of separation W. The results of the analysis, repeated for different values of the angle α, always assuming $k = 2$, are shown in

t_0^I MPa	t_0^{II} MPa	G_{cr}^I $\frac{N}{mm}$	G_{cr}^{II} $\frac{N}{mm}$	K $\frac{N}{mm^3}$
2	4	0.1	0.3	100

Table 3: Non-proportional unloading/reloading path. Adopted cohesive properties.

Figure 15b. The work of separation correctly exhibits a smooth transition from an initial plateau value equal to the fracture energy in mode I to a final one: the initial plateau is due to the fact that Δ_{max} is lower than the elastic limit, i.e. the development of damage occurs only during the pure mode I reloading phase, whereas the final plateau is reached when Δ_{max} is greater than the value of complete decohesion, meaning that the interface is completely broken when the unloading phase starts. The work of separation associated to the final plateau is affected by the choice of the angle α, i.e., as expected, it depends on the interaction between modes.

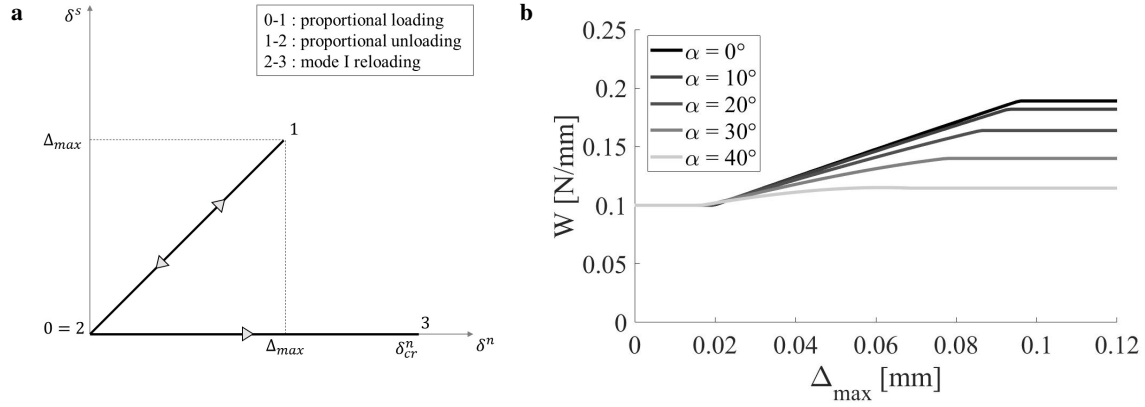

Figure 15: Non-proportional unloading/reloading path. a) Followed path; b) work of separation W vs maximum opening displacement $\Delta_{\max}$ reached at the end of the proportional loading path.

3.4. Sinusoidal path

In this fourth consistency test, proposed in Spring et al. (2016), a mixed-mode loading/unloading path is applied by considering the sinusoidal histories of normal and sliding displacements shown in Figure 16 and described by:

$$\delta^n = 2.0 \text{ mm} \cdot \sin\left(0.15\text{s}^{-1}\tau\right) \tag{47a}$$

$$\delta^s = 3.5 \text{ mm} \cdot \sin\left(0.12\text{s}^{-1}\tau\right) \tag{47b}$$

being τ a time-like parameter ranging from 0 s to 100 s. The test is performed considering the values of peak cohesive stresses and fracture energies in Pure Modes I and II proposed in Spring et al. (2016); the adopted cohesive properties are listed in Table 4. The compressive case is handled by a penalty approach without friction, taking the penalty stiffness equal to K.

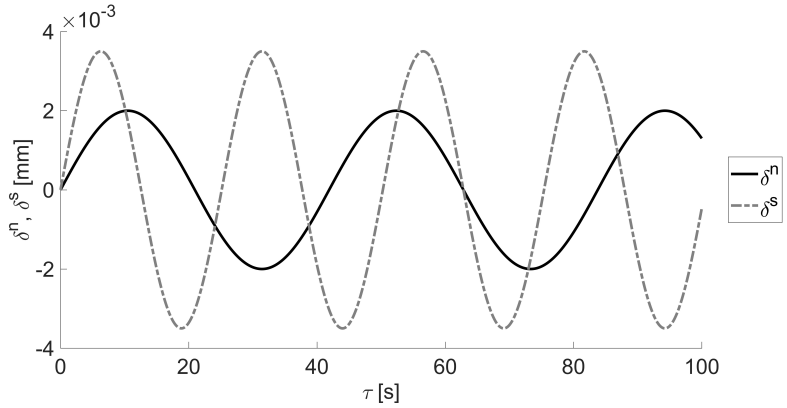

Figure 16: Sinusoidal path. Histories of opening displacements.

t_0^I MPa	t_0^{II} MPa	G_{cr}^I $\frac{N}{mm}$	G_{cr}^{II} $\frac{N}{mm}$	K $\frac{N}{mm^3}$	α deg	k -
40	15	0.1	0.1	11,250	30	2

Table 4: Sinusoidal path. Adopted cohesive properties.

The response of the cohesive model in terms of traction-separation curves is shown in Figure 17. It can be observed that the slope remains constant during the unloading phases, meaning that, as expected, the damage is not increasing.

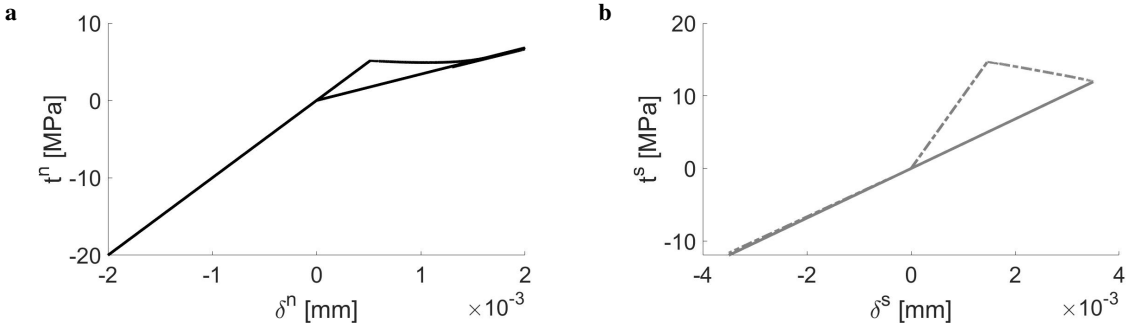

Figure 17: Sinusoidal loading/unloading path. Traction-separation curves.

3.5. Proportional loading with non-proportional unloading

As proposed in Gilormini and Diani (2017), a proportional loading path with $\delta^n = \delta^s$ up to $\delta^n = \delta^s = \Delta = 0.044$ mm is followed by three different unloading paths, namely proportional unloading, normal/tangential unloading and tangential/normal unloading respectively. In the first case, the unloading path coincides with the loading one; in the case of the normal/tangential path, initially the normal opening δ^n is decreased to 0 mm, keeping δ^s constant, and, then, δ^s is decreased to 0 mm; finally, the case of the tangential/normal opening is complementary to the previous one, since the interface is firstly unloaded in the tangential direction keeping δ^n constant and, then, unloaded in the normal direction. The resulting

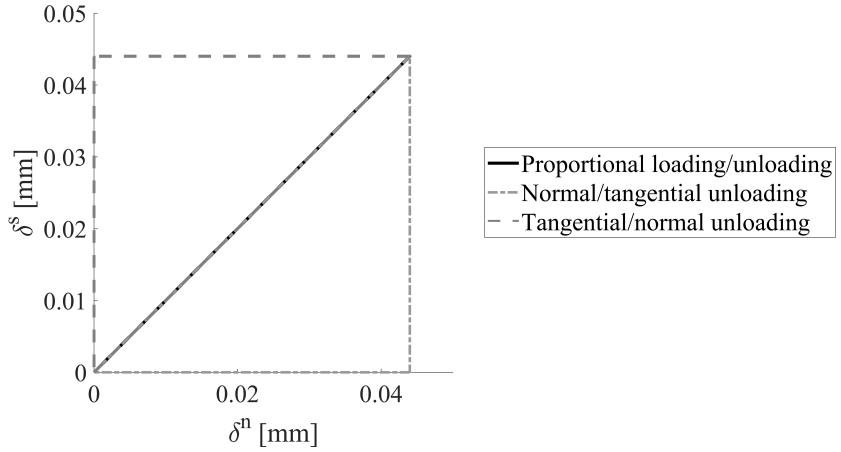

Figure 18: Proportional loading with non-proportional unloading. Proportional unloading (solid black line), normal/tangential unloading (grey dashed line), tangential/normal unloading (grey dash-dot line).

three loading/unloading paths are displayed in Figure 18. The adopted cohesive properties, taken from Gilormini and Diani (2017), are the same of the example described in section 3.3.

The numerical results are compared in Figure 19 showing the traction-separation curves computed for $\alpha = 30°$ and $k = 2$: as expected, the numerical responses in the three cases are perfectly overlapped since the different unloading paths do not affect the resulting traction-separation curves.

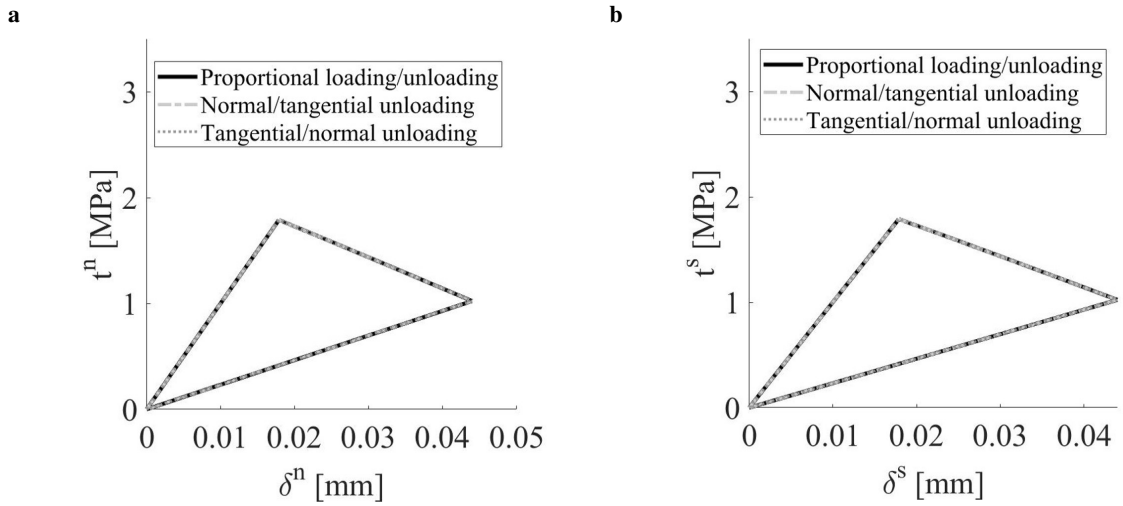

Figure 19: Proportional loading with non proportional unloading. Traction-separation curves.

4. Accuracy tests

In these applications, the experimental data resulting from Mixed Mode Bending (MMB) tests (Reeder and Crews, 1990) performed by different authors on various fiber reinforced composite materials are reproduced to demonstrate the effectiveness of the proposed model in capturing the variation of the fracture energy with the mode-ratio. In detail, the numerical results shown in this section take into account the experimental results obtained by Reeder (1992) for AS4/PEEK, AS4/3501-6 and IM7/977-2,

Material	Reference	G_{cr}^{I} $\frac{mJ}{mm^2}$	G_{cr}^{II} $\frac{mJ}{mm^2}$	t_0^I MPa	t_0^{II} MPa	K $\frac{N}{mm^2}$	α deg	k
AS4/PEEK	Reeder (1992)	0.779	1.142	80	100	10,000	22	1.6
AS4/3501-6	Reeder (1992)	0.090	0.600	45	48	50,000	23	4
IM7/977-2	Reeder (1992)	0.310	1.410	70	130	10,000	20	6
HMF/5322	Adeyemi et al. (1999)	0.3043	0.8039	10	18	10,000	20	10
IM7/8552	Krueger (2012)	0.212	0.774	60	90	20,000	30	6

Table 5: MMB tests. Adopted parameters.

by Adeyemi et al. (1999) for HMF/5322 and by Krueger (2012) for IM7/8552. While the AS4/PEEK has a tougher thermoplastic matrix, with similar mode I and mode II fracture energies, the other three composites have a thermoset matrix, exhibiting substantially different responses.

The adopted cohesive parameters, i.e. the fracture energies G_{cr}^{I}, G_{cr}^{II} and the peak tractions t_0^I, t_0^{II} in pure modes I and II, the internal angle α and the exponent k, are reported in Table 5 for all the considered composite materials. The internal angle α and the exponent k have been optimized so to guarantee the best fitting of the experimental data of fracture energy G_{cr} for the mode-ratio of the available experimental points. Once the parameters α and k have been calibrated, the numerical response is obtained by applying to the interface a sequence of radial paths in the plane $\delta^n - \delta^s$ with ratio $\eta = \delta^s/(\delta^n + \delta^s)$ increasing from 0 (pure mode I) to 1 (pure mode II) with step 0.01. For each proportional loading path, the dissipated energy G_{cr} is computed as the sum of the areas G_{cr}^{n} and G_{cr}^{s} beneath the resulting normal and shear traction-separation curves, while the mode-ratio γ is given by the ratio between G_{cr}^{s} and the overall dissipated energy $G_{cr} = G_{cr}^{n} + G_{cr}^{s}$.

The results obtained for the three fiber-reinforced composites tested by Reeder (1992), namely AS4/PEEK, AS4/3501-6 and IM7/977-2, are shown in Figure 20, in which the numerical prediction of the fracture energy as a function of the mode-ratio is compared with the experimental data and with the curve obtained with the empirical Power Law criterion $\left(\frac{G_{cr}^{n}}{G_{cr}^{I}}\right)^{\alpha} + \left(\frac{G_{cr}^{s}}{G_{cr}^{II}}\right)^{\beta} = 1$, whose exponents have been calibrated by Reeder himself ($\alpha = 1.662$, $\beta = 0.7329$ for AS4/PEEK; $\alpha = 0.0571$, $\beta = 5.039$ for AS4/3501-6; $\alpha = 0.126$, $\beta = 5.447$ for IM7/977-2): the dots corresponds to the experimental points, the red dashed lines are obtained with the Power Law and the solid lines are the results of the present model. The results obtained with the proposed model and with the Power Law are of comparable accuracy. However, it should be emphasized that the latter case is the result of a curve fitting, while in our case the curves have been obtained by integration along the prescribed loading path and, therefore, it is expected that a similar accuracy could be obtained also along different, more complex loading paths. The same results are also plotted in Figure 21 using a different but common representation in terms of the contributions of G_{cr}^{n} and G_{cr}^{s} to the total fracture energy. The very good accuracy and flexibility of the model can be appreciated also with this different visualization.

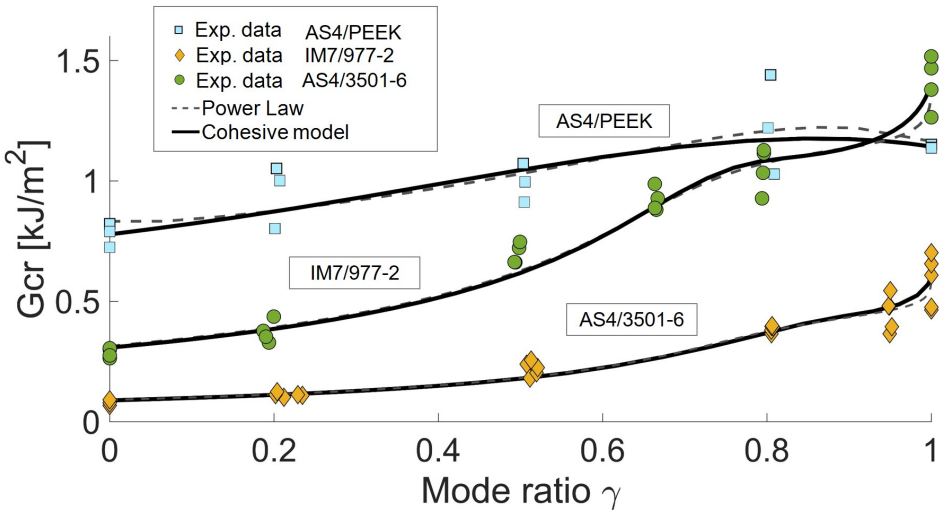

Figure 20: MMB tests. Experimental vs numerical mixed-mode fracture energies. Total fracture energy evolution with mode-ratio. Dots: experimental data (Reeder, 1992). Dashed line: Power Law (Reeder, 1992). Solid black lines: results of the present model.

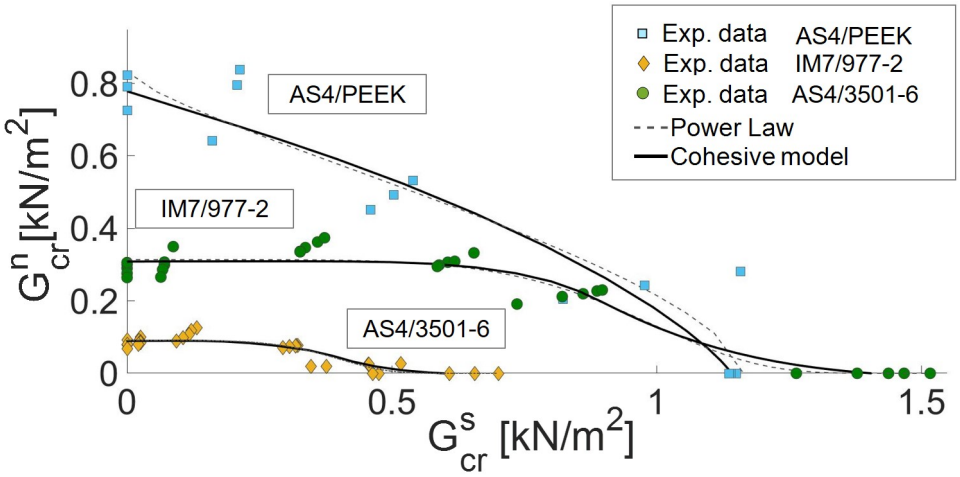

Figure 21: MMB tests. Experimental vs numerical mixed-mode fracture energies. Normal and shear contributions to the total fracture energy. Dots: experimental data (Reeder, 1992). Dashed line: Power Law (Reeder, 1992). Solid black lines: results of the present model.

Figure 22 shows the results obtained for IM7/8552: the numerical response (black solid line) with the proposed model is depicted together with the experimental points (grey dots) reported in Krueger (2012) and, for comparison purposes, with the fitting curve obtained with the empirical Benzeggagh-Kenane (B-K) law (Benzeggagh and Kenane, 1996) $G_{cr} = G^I_{cr} + \left(G^{II}_{cr} - G^I_{cr}\right)\left(\frac{G^s_{cr}}{G^n_{cr}+G^s_{cr}}\right)^{\eta}$ (dashed grey line), with the exponent $\eta = 2.1$ calibrated by Krueger himself to fit the experimental data.

Finally, the results obtained for HMF/5322 are presented in Figure 23, solid curve: also in this case, a good agreement between the experimental data and the curve obtained with the proposed cohesive law can be observed. As noted in section 2.3, the classical free energy decomposition in normal and shear components is recovered by setting $\alpha = 0$, while a quadratic damage initiation condition in terms of tractions is obtained by also setting $k = 1$. The results obtained in this case using the classical

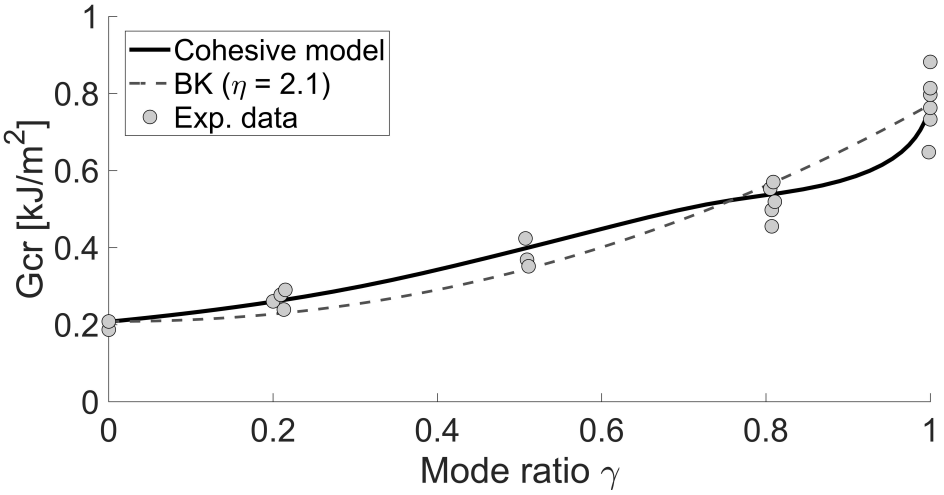

Figure 22: MMB tests. IM7/8552. Experimental vs numerical mixed-mode fracture energies. Dots: experimental data (Krueger, 2012). Dashed line: B-K law (Benzeggagh and Kenane, 1996). Solid black line: result of the present model.

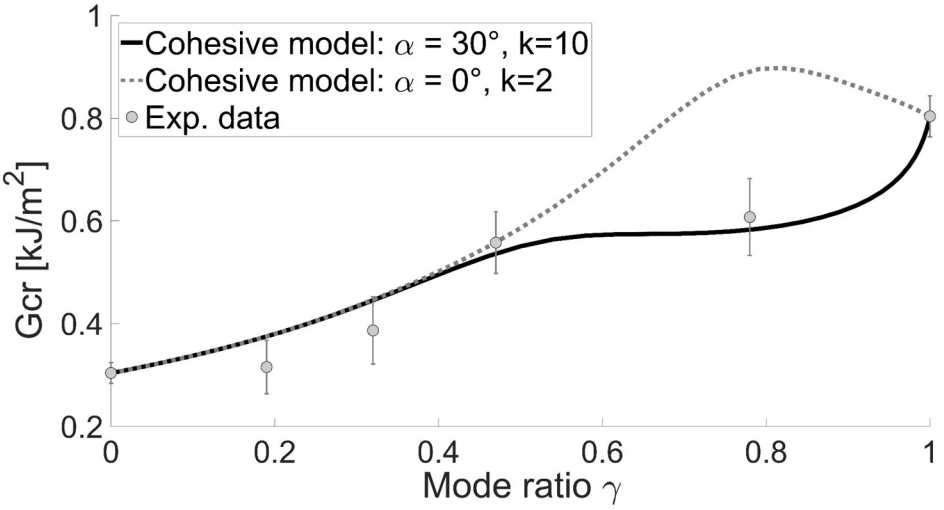

Figure 23: MMB tests. HMF/5322. Experimental vs numerical mixed-mode fracture energies. Dots: experimental data (Adeyemi et al., 1999). Solid line: result of the present model with parameters from Table 5. Dashed line: result of the present model with $\alpha = 0$ and $k = 2$.

decomposition are shown in Figure 23, dashed curve, where it can be observed that the model completely fails to reproduce the response for high mode ratio.

In all the cases considered in this section, the cohesive model is able to reproduce correctly the growth of the fracture energy with the mode-ratio: the numerical curves are always in good agreement with the experimental data, even though different composite materials, with substantially different evolution of the fracture energy with the mode-ratio, have been analyzed, confirming the generality and robustness of the model. Furthermore, the numerical results are very close to the best-fitting obtained with the Power Law in the case of AS4/PEEK, AS4/3501-6 and IM7/977-2, while in the case of IM7/8552 the cohesive model provides a response more accurate than the best fitting obtained by means of the B-K criterion.

E_{11}	$E_{22} = E_{33}$	$\nu_{12} = \nu_{13}$	$G_{12} = G_{13}$	G_{23}
MPa	MPa	-	MPa	MPa
131,700	8,800	0.3	4,600	3,700

Table 6: T300/913. Elastic properties.

5. Evolutionary tests

The proposed cohesive model has been used as constitutive law for a 4-node zero-thickness decohesion element implemented in a user-written element subroutine (VUEL) for the commercial finite element software Abaqus/Explicit. The implementation has been validated against the simulation of three experimental tests, namely a double cantilever beam (DCB) test, a mixed mode bending (MMB) test and a four points bend end-notched flexure (4ENF) test, performed by Pinho and reported in Pinho (2005) and Pinho et al. (2006). All the samples were made of a 24-ply unidirectional carbon-epoxy T300/913 laminate with overall thickness equal to 3.1 mm and width $B = 20$ mm. In all the cases, a pre-crack with variable length depending on the test type was introduced in the specimen. The material has been modeled as orthotropic linear elastic. The mechanical properties of the laminate, taken from Pinho (2005), are reported in Table 6, while Table 7 summarizes the adopted cohesive models. The parameters α and k have been identified on the basis of the experimental data provided in Pinho et al. (2006). Figure 24 shows the outcome of the identification procedure, comparing the experimental points in terms of fracture energy vs mode-ratio with the numerical curve obtained by applying to the interface a sequence of proportional loading paths with mode-ratio increasing from 0 to 1: as in the previous cases, the numerical prediction is in very good agreement with the experimental data.

Although the fracture energy data reported in Pinho et al. (2006) correspond to a series of MMB tests performed at three different mode-ratios (namely, 0.20, 0.52 and 0.81), together with the two pure modes tests, the load-displacement responses are available only for the DCB, for the 4ENF and for the MMB test with mode-ratio equal to 0.52. The finite element simulations in this section therefore consider only these three tests.

In all cases, the problem has been discretized by means of 4-node plane-strain elements and zero-thickness 4-node cohesive elements placed in the middle plane of the specimen to simulate its progressive delamination. Since the specimens are made of a unidirectional composite material, only two plies, having thickness equal to 1.55 mm and fiber orientation parallel to the longitudinal direction of the sample, are introduced in the model, separated by the interface layer. The presence of the initial notch is accounted for by introducing open decohesion elements, i.e. interface elements capable to deal with contact by means of a penalty approach, to avoid interpenetration of the arms. The mesh is characterized by five elements through-the-thickness per lamina. The discretization is more refined in the zone where the decohesion is expected to develop, with a minimum length of the interface elements equal to 0.125

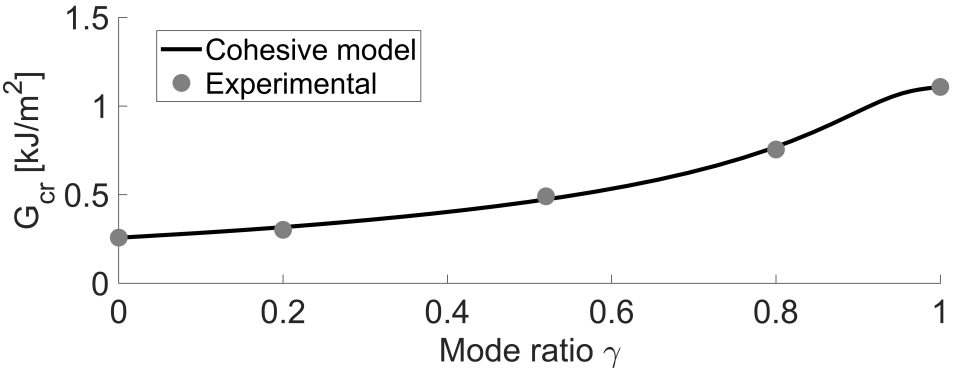

Figure 24: MMB tests. T300/913. Experimental vs numerical mixed-mode fracture energies. Dots: experimental data. Solid black line: result of the present model.

t_0^I MPa	t_0^{II} MPa	G_{cr}^I $\frac{N}{mm}$	G_{cr}^{II} $\frac{N}{mm}$	K $\frac{N}{mm^3}$	α	k -
65	75	0.258	1.108	10,000	27.5	4

Table 7: T300/913. Cohesive properties.

mm increasing up to 0.25 mm far from it. This is compatible with the roughly estimated characteristic lengths of the cohesive process zone.

Since an explicit algorithm is adopted to simulate a quasi-static phenomenon (delamination tests are performed at slow speed), Rayleigh damping with a mass proportional coefficient $\alpha = 0.001$ s^{-1} and a stiffness proportional coefficient $\beta = 10^{-7}$ s have been introduced to reduce the oscillations.

5.1. Double cantilever beam test (DCB)

The DCB configuration is shown in Figure 25: the specimen is 140 mm long and has an initial notch length a_0 equal to 53 mm. Two opposite vertical displacements, linearly increasing in time from 0 mm to 10 mm with a displacement rate equal to 10 mm/s, are imposed to the notched ends of the specimen, while the opposite end is held fixed. The outcome of the numerical simulation is shown in Figure 26, in which the load - opening displacement curve, obtained recording the reaction force at point A, is compared with the experimental data reported in Pinho et al. (2006): the numerical prediction perfectly matches the experimental points up to an opening displacement equal to 8 mm and, then, slightly underestimates the experimental load, even if it is able to capture the overall softening trend.

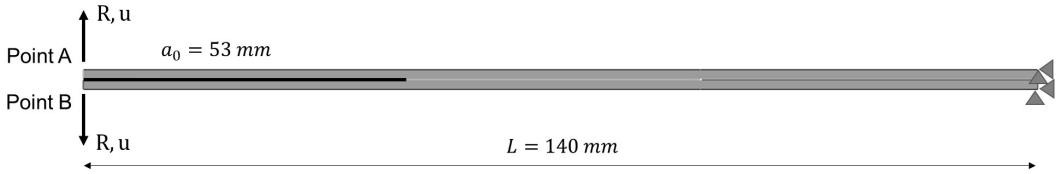

Figure 25: DCB test. Geometry, boundary and loading conditions.

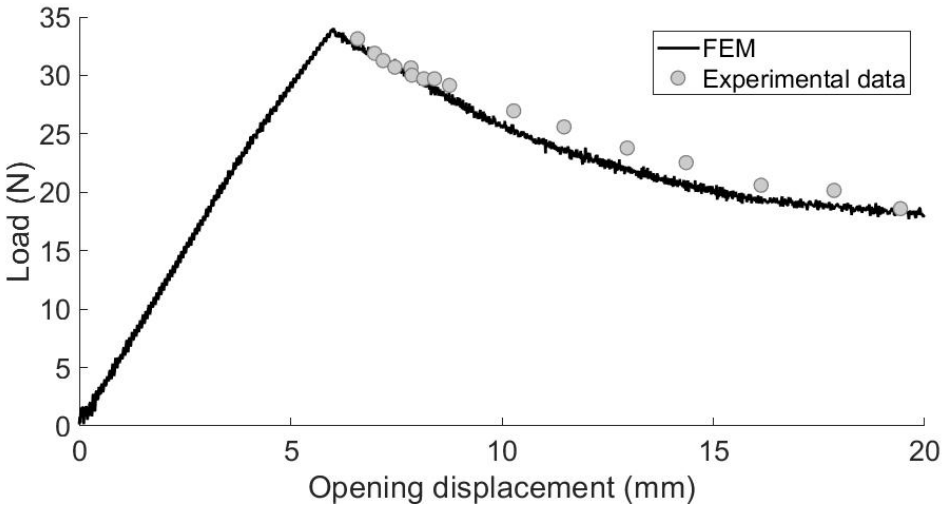

Figure 26: DCB test. Comparison with experimental data.

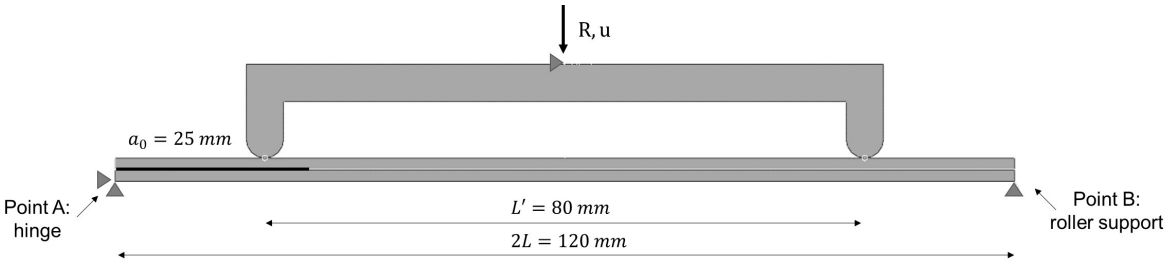

Figure 27: 4ENF test. Geometry, boundary and loading conditions.

5.2. Four points bend end-notched flexure test (4ENF)

The specimen is 120 mm long and the pre-crack length is equal to 25 mm. As suggested in Pinho et al. (2006), part of the loading rig is explicitly introduced in the model in order to properly reproduce the loading conditions of the experimental test: the loading lever is modeled as a rigid body and connected to the upper lamina by means of two contact conditions to simulate the presence of rollers in the experimental setup. The geometry of the test setup considered for the simulation is depicted in Figure 27, together with the boundary and loading conditions adopted for the numerical analysis. The bottom lamina is held fixed by a hinge (point A) and by a roller support (point B). A downward vertical displacement u, linearly increasing in time from 0 mm to 3.5 mm, for a duration of 1 s, is imposed to the rigid loading lever. Figure 28 shows the adopted discretization, magnifying a detail of the mesh in the more refined zone. Contact between the free sides of the initial notch has been dealt with using the contact features available in Abaqus. The notch tip region remains in almost perfect pure mode II condition throughout the analysis, with negligible normal stresses, as it has been verified by checking the output of the finite element simulation.

The comparison between the numerical prediction in terms of load-displacement response and the experimental data reported in Pinho et al. (2006) is shown in Figure 29. The simulation result is in very

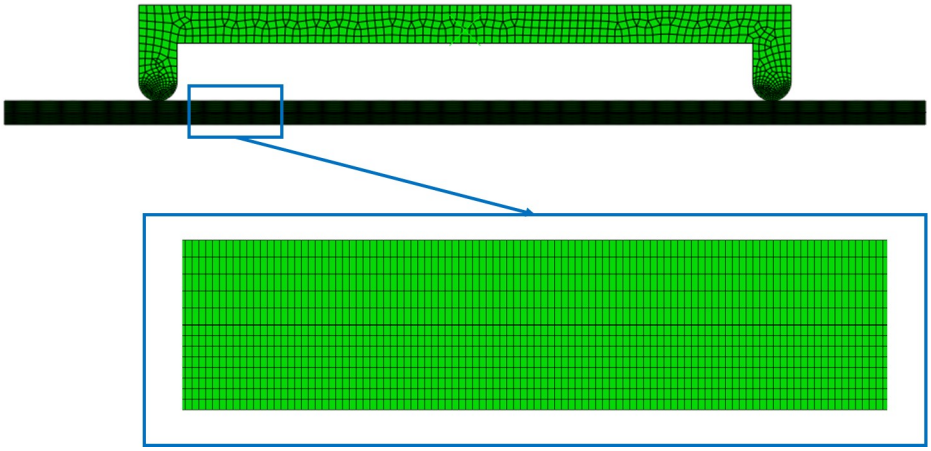

Figure 28: 4ENF test. Adopted mesh.

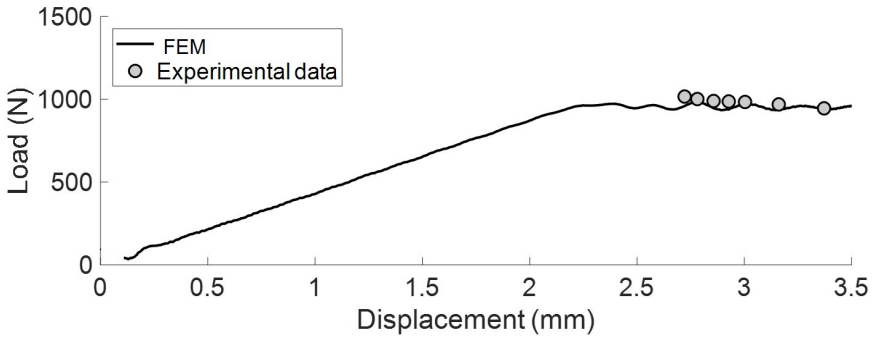

Figure 29: 4ENF. Load-displacement response. Comparison with experimental data.

good agreement with the available experimental points.

5.3. Mixed-mode bending test (MMB)

Figure 30 depicts the considered geometry: the specimen is 120 mm long and its initial pre-crack length is equal to 33 mm. The bottom supports are simulated by prescribing a roller at point D and an hinge at point C. The loading arm, modeled as a rigid body, has an overall length $L + c$, being $c = 51$ mm the length of the lever arm and $L = 60$ mm, and is connected to the specimen by a bilateral tie interaction prescribed at point A and a unilateral contact condition imposed at point B, reproducing the presence of a hinged connection and a roller between the loading lever and the sample in the experimental setup. The adopted discretization is shown in Figure 31. The simulation is performed by imposing a downward vertical displacement u at point E of the lever arm, linearly increasing in time up to 7 mm for a duration of 1 s. The numerical response in terms of load vs displacement is then obtained recording the reaction force at that point. The comparison with the experimental data provided in Pinho et al. (2006) is shown in Figure 32. The finite element simulation is able to reproduce the experimental softening branch, even though the numerical response is affected by an oscillatory behavior due to the explicit integration scheme.

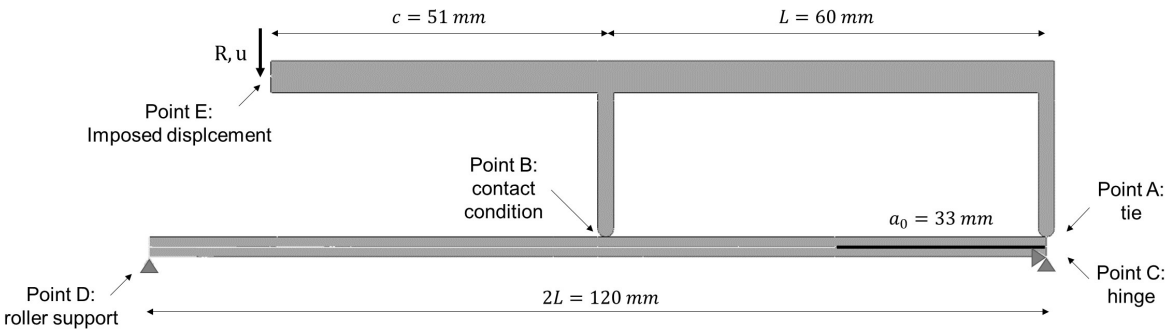

Figure 30: MMB test. Geometry, boundary and loading conditions.

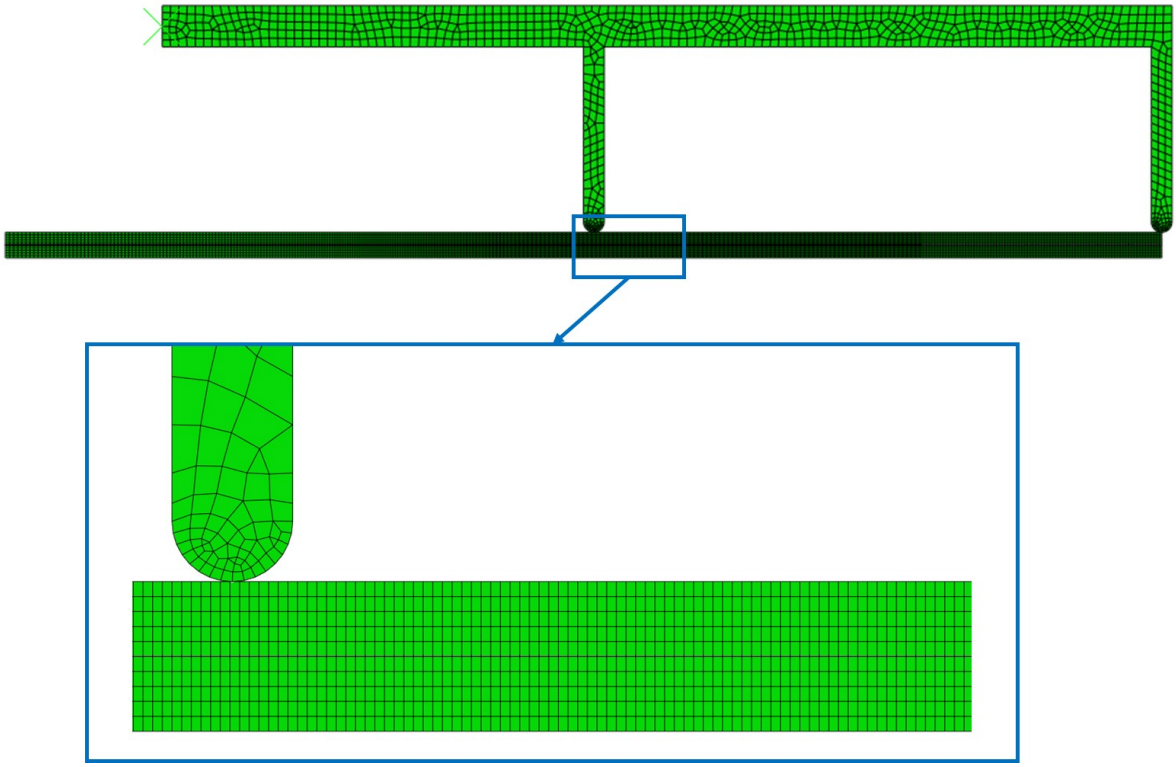

Figure 31: MMB test. Adopted discretization.

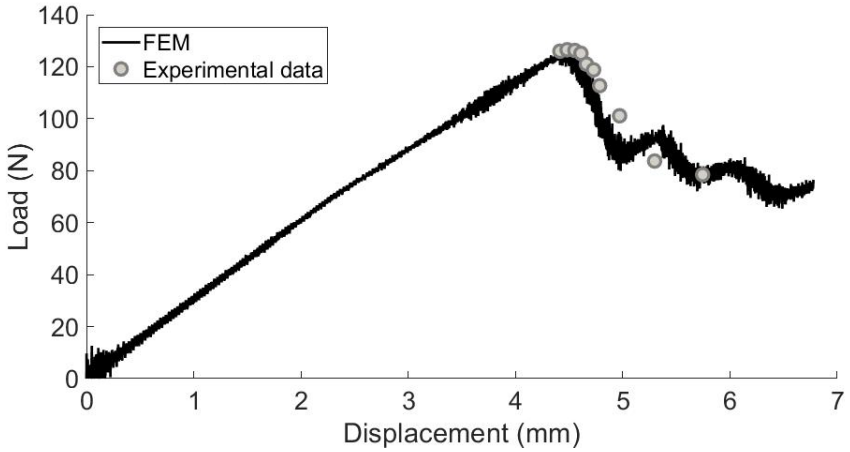

Figure 32: MMB test. Load-displacement response. Comparison with experimental data.

6. Conclusions

A new framework for the formulation of cohesive mixed mode delamination models, based on a thermodynamically consistent isotropic damage formulation, has been presented. The new main ingredient is the decomposition of the free energy density based on the definition of three damage modes in the plane of normal and shear tractions. The definition of the damage modes is motivated by the observation of the shape of the failure domains of different types of interfaces and is used to construct in a rational and effective way the damage activation function.

Advantages of the proposed model with respect to other existing models are:

- rational and physically motivated definition of the damage activation function, which is simply obtained by comparison of the driving forces acting on the individual damage modes with their current thresholds;
- any form of the traction-separation laws can be incorporated in the proposed framework;
- the traction-separation law in mixed-mode is the result of the definition of the traction-separation laws in the pure modes only, with different types of traction-separation law that can be adopted for mode I and mode II, so that different responses, with different fracture energies, can be easily accounted for in mode I and II;
- no definition of equivalent tractions or opening displacements is required by the model;
- no assumptions on the evolution of the fracture energy with the mode-ratio are made a priori, as it is the case, e.g., when the Benzeggagh-Kenane (Benzeggagh and Kenane, 1996) or the Power-Law (Reeder, 1992) interpolations are adopted. The fracture energy evolution is simply obtained as an outcome of the interaction between modes along the prescribed loading path;
- no assumptions on the loading path are necessary: radial loading and non-proportional loading with arbitrary loading/unloading are treated by the model in an equally consistent way;
- in the considered bilinear form, the model requires only few parameters: the elastic stiffness, the parameters characterizing the traction-separation laws in the pure modes I and II, the internal angle α and the exponent k;
- the model dictates a simple and rational parameter identification strategy: parameters characterizing the traction-separation laws in the pure modes are identified first, based on tests in pure mode I and II. The parameters α and k are then identified based on mixed-mode tests such as the MMB test, for varying mode-ratio.

The case of bilinear traction-separation laws in the pure modes has been investigated in detail. Even though the softening branch is linear in the pure modes, it has been shown that a nonlinear softening branch is in general obtained under mixed-mode loading conditions.

Despite its simplicity, the model has been shown to be sufficiently robust and general to accurately reproduce the mixed-mode delamination behavior of an unusually wide range of different interfaces, along any type of proportional and non-proportional loading paths. A particularly exhaustive and rigorous validation protocol for delamination models has been proposed and it has been adopted for the model validation. The model consistency and accuracy, together with its capability to reproduce the evolutionary interface behavior for different mixed-mode loading conditions, have been validated by means of several delamination tests proposed in the literature, also allowing to elucidate the role played by the internal angle α in the case of complex, non-proportional paths. The model has also been implemented as a user material routine in the finite element code Abaqus Explicit and has been used to simulate mixed-mode delamination tests proposed in the literature, obtaining very accurate results for all mode-ratios.

Appendix A.

Appendix A.1. Radial path with different properties in the pure modes

Let us consider a radial path, of the type discussed in section 3.1, with components δ^n and δ^s proportional, through the mode-ratio parameter η, to a monotonically growing opening factor δ. Substituting the expressions (43) of δ^n and δ^s in terms of η and δ, the driving forces Y^i in equations (15) become

$$\begin{aligned}
Y^{1,\eta} &= \frac{1}{2} t_0^I \delta_0^I \left(1 - \frac{t_0^{II}\delta_0^{II}}{t_0^I \delta_0^I} \tan^2\alpha\right)\left[\frac{1-\eta}{\delta_0^I}\right]^2 \delta^2 \\
Y^{2,\eta} &= \frac{1}{4} t_0^{II} \delta_0^{II} \left[\left(\frac{\eta}{\delta_0^{II}}\right)^2 + \tan^2\alpha \left(\frac{1-\eta}{\delta_0^I}\right)^2 + 2\frac{(1-\eta)\eta}{\delta_0^I \delta_0^{II}} \tan\alpha\right]\delta^2 \\
Y^{3,\eta} &= \frac{1}{4} t_0^{II} \delta_0^{II} \left[\left(\frac{\eta}{\delta_0^{II}}\right)^2 + \tan^2\alpha \left(\frac{1-\eta}{\delta_0^I}\right)^2 - 2\frac{(1-\eta)\eta}{\delta_0^I \delta_0^{II}} \tan\alpha\right]\delta^2
\end{aligned} \tag{A.1}$$

Defining with the symbol δ_0 the value of δ at first damage activation and enforcing the activation condition $\varphi = 0$, with φ defined in (21), for $\delta \geq \delta_0$, i.e.

$$\varphi = \left(\frac{Y^{1,\eta}}{\chi_0^1 + \chi^1(d)}\right)^k + \left(\frac{Y^{2,\eta}}{\chi_0^2 + \chi^2(d)}\right)^k + \left(\frac{Y^{3,\eta}}{\chi_0^3 + \chi^3(d)}\right)^k - 1 = 0 \tag{A.2}$$

allows to derive the expression of $\delta \geq \delta_0$ along the softening branch as a function of damage:

$$\delta(d,\eta) = \frac{1}{[f(d,\eta)]^{\frac{1}{2k}}} \tag{A.3}$$

with:

$$f(d,\eta) = \left\{ \left(\frac{1-\eta}{\delta_0^I}\right)^2 \frac{\left[1 - \left(\frac{\delta_{cr}^I}{\delta_{cr}^{II}} \frac{\delta_{cr}^{II} - (\delta_{cr}^{II} - \delta_0^{II})d}{\delta_{cr}^I - (\delta_{cr}^I - \delta_0^I)d} \tan\alpha\right)^{2k}\right]^{\frac{1}{k}}}{\left[\frac{\delta_{cr}^I}{\delta_{cr}^I - (\delta_{cr}^I - \delta_0^I)d}\right]^2} \right\}^k + \\ + \left\{ \frac{\left[\left(\frac{\eta}{\delta_0^{II}}\right)^2 + \left(\frac{1-\eta}{\delta_0^I}\right)^2 \tan^2\alpha + 2\frac{(1-\eta)\eta}{\delta_0^I \delta_0^{II}} \tan\alpha\right]}{2^{\frac{1}{k}} \frac{\delta_{cr}^{II}}{\left[\delta_{cr}^{II} - (\delta_{cr}^{II} - \delta_0^{II})d\right]^2}} \right\}^k + \left\{ \frac{\left[\left(\frac{\eta}{\delta_0^{II}}\right)^2 + \left(\frac{1-\eta}{\delta_0^I}\right)^2 \tan^2\alpha - 2\frac{(1-\eta)\eta}{\delta_0^I \delta_0^{II}} \tan\alpha\right]}{2^{\frac{1}{k}} \frac{\delta_{cr}^{II}}{\left[\delta_{cr}^{II} - (\delta_{cr}^{II} - \delta_0^{II})d\right]^2}} \right\}^k \quad \text{(A.4)}$$

The value δ_0 of δ at first activation is then obtained as

$$\delta_0(\eta) = \delta(0,\eta) = \frac{1}{[f(0,\eta)]^{\frac{1}{2k}}} = \frac{1}{[f_0]^{\frac{1}{2k}}} \quad \text{(A.5)}$$

where the expression of f_0 is obtained by setting $\chi^1(d) = \chi^2(d) = \chi^3(d) = 0$ and introducing the expressions (23) and (22) of χ_0^1, χ_0^2 and χ_0^3 in (A.4)

$$f_0 = f(0,\eta) = \left\{ \left[1 - (\tan\alpha)^{2k}\right]^{\frac{1}{k}} \left(\frac{1-\eta}{\delta_0^I}\right)^2 \right\}^k + \\ + \left\{ \frac{1}{2^{\frac{1}{k}}} \left[\left(\frac{\eta}{\delta_0^{II}}\right)^2 + \left(\frac{1-\eta}{\delta_0^I}\right)^2 \tan^2\alpha + 2\frac{(1-\eta)\eta}{\delta_0^I \delta_0^{II}} \tan\alpha\right] \right\}^k + \\ + \left\{ \frac{1}{2^{\frac{1}{k}}} \left[\left(\frac{\eta}{\delta_0^{II}}\right)^2 + \left(\frac{1-\eta}{\delta_0^I}\right)^2 \tan^2\alpha - 2\frac{(1-\eta)\eta}{\delta_0^I \delta_0^{II}} \tan\alpha\right] \right\}^k \quad \text{(A.6)}$$

It should be noted that from the expression (A.5) of δ_0, using equation (43) one could obtain analytically the values of δ^n and δ^s at first damage activation under radial loading for varying mode ratio η. Replacing these values into the elastic relation (7), one could also obtain in parametric form the analytical expression of the curve defining the boundary of the elastic domain, as in Figure 4.

In a way similar to what has been done for δ_0, the critical value δ_{cr} at complete decohesion can be expressed as a function of damage by setting

$$\delta_{cr}(\eta) = \delta(1,\eta) = \frac{1}{[f(1,\eta)]^{\frac{1}{2k}}} = \frac{1}{[f_{cr}]^{\frac{1}{2k}}} \quad \text{(A.7)}$$

where f_{cr} is obtained by introducing the expressions (40) of $\chi_{cr}^1, \chi_{cr}^2 = \chi_{cr}^3$ in (A.4):

$$f_{cr} = f(1,\eta) = \left\{ \left(\frac{1-\eta}{\delta_0^I} \right)^2 \frac{\left[1 - \left(\frac{\delta_{cr}^I}{\delta_{cr}^{II}} \frac{\delta_0^{II}}{\delta_0^I} \tan\alpha \right)^{2k} \right]^{\frac{1}{k}}}{\left[\frac{\delta_{cr}^I}{\delta_0^I} \right]^2} \right\}^k +$$
$$+ \left\{ \frac{\left[\left(\frac{\eta}{\delta_0^{II}} \right)^2 + \left(\frac{1-\eta}{\delta_0^I} \right)^2 \tan^2\alpha + 2\frac{(1-\eta)\eta}{\delta_0^I \delta_0^{II}} \tan\alpha \right]}{2^{\frac{1}{k}} \left[\frac{\delta_{cr}^{II}}{\delta_0^{II}} \right]^2} \right\}^k + \left\{ \frac{\left[\left(\frac{\eta}{\delta_0^{II}} \right)^2 + \left(\frac{1-\eta}{\delta_0^I} \right)^2 \tan^2\alpha - 2\frac{(1-\eta)\eta}{\delta_0^I \delta_0^{II}} \tan\alpha \right]}{2^{\frac{1}{k}} \left[\frac{\delta_{cr}^{II}}{\delta_0^{II}} \right]^2} \right\}^k \tag{A.8}$$

The fracture energy along a radial path can be obtained by integrating the dissipation rate (30) up to $d = 1$ (complete decohesion), after replacing δ in (A.1) with its expression (A.3) as a function of damage:

$$G_{cr}(\eta) = \int_0^1 Y(d,\eta) d(d) = \int_0^1 \left(Y^{1,\eta}(d,\eta) + Y^{2,\eta}(d,\eta) + Y^{3,\eta}(d,\eta) \right) d(d) \tag{A.9}$$

Appendix A.2. Radial path with equal properties in the pure modes

In the special case of equal properties in the pure modes, i.e. $t_0^I = t_0^{II} = \hat{t}_0$, $\delta_0^I = \delta_0^{II} = \hat{\delta}_0$, $\delta_{cr}^I = \delta_{cr}^{II} = \hat{\delta}_{cr}$, $G_{cr}^I = G_{cr}^{II}$ ($\hat{\delta}_0$ and $\hat{\delta}_{cr}$ not to be confused with δ_0 and δ_{cr}, values of the loading parameter δ at first damage activation and at complete decohesion, respectively), the expressions in the previous section can be further simplified. With the following definitions:

$$\bar{\delta} = \frac{\delta}{\hat{\delta}_0}, \quad \bar{\delta}^n = (1-\eta)\bar{\delta}, \quad \bar{\delta}^s = \eta\bar{\delta} \tag{A.10}$$

the driving forces $Y^{i,\eta}$ in (A.1) take the form

$$\begin{aligned} Y^{1,\eta} &= \frac{1}{2}\hat{t}_0\hat{\delta}_0 \left(1 - \tan^2\alpha\right)(1-\eta)^2 \bar{\delta}^2 \\ Y^{2,\eta} &= \frac{1}{4}\hat{t}_0\hat{\delta}_0 \left[\eta + (1-\eta)\tan\alpha\right]^2 \bar{\delta}^2 \\ Y^{3,\eta} &= \frac{1}{4}\hat{t}_0\hat{\delta}_0 \left[\eta - (1-\eta)\tan\alpha\right]^2 \bar{\delta}^2 \end{aligned} \tag{A.11}$$

while the initial thresholds $\chi_0^1, \chi_0^2, \chi_0^3$ in (23) and (22) and the internal variables χ^1, χ^2, χ^3 in (39) and (35) become

$$\begin{aligned} \chi_0^1 &= \frac{1}{2}\hat{t}_0\hat{\delta}_0 \frac{1 - \tan^2\alpha}{\left[1 - (\tan^2\alpha)^k\right]^{\frac{1}{k}}}, & \chi^1 &= \chi_0^1 \left\{ \left[\frac{\hat{\delta}_{cr}}{\hat{\delta}_{cr} - (\hat{\delta}_{cr} - \hat{\delta}_0)d} \right]^2 - 1 \right\} \\ \chi_0^2 &= \chi_0^3 = 2^{\frac{1}{k}} \frac{1}{4}\hat{t}_0\hat{\delta}_0, & \chi^2 &= \chi^3 = \chi_0^2 \left\{ \left[\frac{\hat{\delta}_{cr}}{\hat{\delta}_{cr} - (\hat{\delta}_{cr} - \hat{\delta}_0)d} \right]^2 - 1 \right\} \end{aligned} \tag{A.12}$$

Introducing these expressions in (A.2), the loading parameter $\delta(d,\eta)$ can be expressed in the form (A.3), where $f(d,\eta)$ is given by

$$f(d,\eta) = \frac{1}{\hat{\delta}_0^{2k}} \left(\frac{\hat{\delta}_{cr} - (\hat{\delta}_{cr} - \hat{\delta}_0)d}{\hat{\delta}_{cr}} \right)^{2k} g(\eta)^{-2k} \tag{A.13}$$

with

$$g(\eta) = \left\{ \left(1 - \tan^{2k}\alpha\right)(1-\eta)^{2k} + \frac{1}{2}\left[\eta + (1-\eta)\tan\alpha\right]^{2k} + \frac{1}{2}\left[\eta - (1-\eta)\tan\alpha\right]^{2k} \right\}^{-\frac{1}{2k}},$$

$$g(0) = g(1) = 1 \tag{A.14}$$

In the special case of the exponent $k = 2$, $g(\eta)$ simplifies to

$$g(\eta) = \left[(1-\eta)^4 + 6\eta^2(1-\eta)^2\tan^2\alpha + \eta^4\right]^{-\frac{1}{4}} \tag{A.15}$$

and it becomes symmetric with respect to $\eta = 0.5$, i.e. $g(\eta) = g(1-\eta)$. If in addition to $k = 2$, $\alpha = 30°$ is assumed in (A.14), one has $\tan\alpha = \sqrt{3}/3$ and

$$g(\eta) = \left[(1-\eta)^2 + \eta^2\right]^{-\frac{1}{2}} \tag{A.16}$$

Using (A.13) in (A.3), the loading parameter δ, for $\delta \geq \delta_0(\eta)$ is finally written as

$$\delta = \hat{\delta}_0 \left(\frac{\hat{\delta}_{cr}}{\hat{\delta}_{cr} - (\hat{\delta}_{cr} - \hat{\delta}_0)d} \right) g(\eta), \quad \delta \geq \delta_0(\eta) \tag{A.17}$$

The values $\delta_0(\eta)$ and $\delta_{cr}(\eta)$, the latter being the value of δ at complete decohesion, can be easily obtained by setting $d = 0$ and $d = 1$ in (A.17)

$$\delta_0(\eta) = \hat{\delta}_0 g(\eta), \quad \delta_{cr}(\eta) = \hat{\delta}_{cr} g(\eta) \tag{A.18}$$

The expression (A.17) can be inverted, solving for the damage d as a function of δ:

$$d(\delta) = \frac{\hat{\delta}_{cr}}{\hat{\delta}_{cr} - \hat{\delta}_0} \left(1 - \frac{\hat{\delta}_0}{\delta} g(\eta) \right), \quad \delta \geq \delta_0(\eta) \tag{A.19}$$

Since the tractions in a radial loading path are given by

$$t^n = (1-d)K(1-\eta)\delta, \quad t^s = (1-d)K\eta\delta \tag{A.20}$$

replacing (A.19) in (A.20), one obtains for $\delta \geq \delta_0(\eta)$

$$t^n = K(1-\eta)\left(1 - \frac{\hat{\delta}_{cr}}{\hat{\delta}_{cr} - \hat{\delta}_0}\right)\delta + K(1-\eta)\frac{\hat{\delta}_0\hat{\delta}_{cr}}{\hat{\delta}_{cr} - \hat{\delta}_0}g(\eta)$$
$$t^s = K\eta\left(1 - \frac{\hat{\delta}_{cr}}{\hat{\delta}_{cr} - \hat{\delta}_0}\right)\delta + K\eta\frac{\hat{\delta}_0\hat{\delta}_{cr}}{\hat{\delta}_{cr} - \hat{\delta}_0}g(\eta) \tag{A.21}$$

The second term on the r.h.s of both equations in (A.21) is constant and varies only with the mode-ratio η, which means that for $\delta \geq \delta_0(\eta)$ the softening branch, under mixed-mode radial loading and equal properties in the pure modes, is always linear, whatever is the mode-ratio. This is in contrast with the general case of different properties in the pure modes, for which the softening branch is linear only under pure mode I or II loading conditions.

In this special case of equal properties, the fracture energy can be easily computed analytically as a function of the mode-ratio η:

$$G_{cr}(\eta) = \frac{1}{2}t_0^n(\eta)\delta_{cr}^n(\eta) + \frac{1}{2}t_0^s(\eta)\delta_{cr}^s(\eta) = \frac{1}{2}K\delta_0\delta_{cr}[(1-\eta)^2 + \eta^2] = \frac{1}{2}K\hat{\delta}_0\hat{\delta}_{cr}g^2(\eta)[(1-\eta)^2 + \eta^2] \tag{A.22}$$

(We recall that t_0^n and t_0^s denote the tractions peak values for the considered mixed-mode path, not to be confused with their corresponding values t_0^I, t_0^{II} in the pure modes. Similar distinctions apply to δ_{cr}^n, δ_{cr}^s and δ_{cr}^I, δ_{cr}^{II}).

Acknowledgments

The financial support by Tetra Pak Packaging Solutions is kindly acknowledged.

References

Adeyemi NB, Shivakumar KN, Avva VS. Delamination fracture toughness of woven-fabric composites under mixed-mode loading. AIAA journal 1999;37(4):517–20. doi:10.2514/2.747.

Alfano G, Crisfield MA. Finite element interface models for the delamination analysis of laminated composites: mechanical and computational issues. International Journal for Numerical Methods in Engineering 2001;50(7):1701–36. doi:10.1002/nme.93.

Alfano G, Sacco E. Combining interface damage and friction in a cohesive-zone model. Int J Numer Meth Engng 2006;68(5):542–82. doi:10.1002/nme.1728.

Allix O, Corigliano A. Modeling and simulation of crack propagation in mixed-modes interlaminar fracture specimens. International Journal of Fracture 1996;77(2):111–40. doi:10.1007/bf00037233.

Benzeggagh ML, Kenane M. Measurement of mixed-mode delamination fracture toughness of unidirectional glass/epoxy composites with mixed-mode bending apparatus. Composites Science and Technology 1996;56(4):439–49. doi:10.1016/0266-3538(96)00005-x.

Borgqvist E, Wallin M, Ristinmaa M, Tryding J. An anisotropic in-plane and out-of-plane elasto-plastic continuum model for paperboard. Composite Structures 2015;126:184–95. doi:10.1016/j.compstruct.2015.02.067.

van den Bosch MJ, Schreurs PJG, Geers MGD. An improved description of the exponential Xu and Needleman cohesive zone law for mixed-mode decohesion. Engineering Fracture Mechanics 2006;73(9). doi:10.1016/j.engfracmech.2005.12.006.

Camanho PP, Davila CG, de Moura MF. Numerical simulation of Mixed-Mode progressive delamination in composite materials. Journal of Composite Materials 2003;37(16):1415–38. doi:10.1177/0021998303034505.

Carol I, Prat PC, López CM. Normal/Shear cracking model: Application to discrete crack analysis. Journal of Engineering Mechanics 1997;123(8):765–73. doi:10.1061/(asce)0733-9399(1997)123:8(765).

Cocchetti G, Maier G, Shen XP. Interface and joint models, piecewise linearisation, time-integration. Computer Modeling in Engineering & Sciences 2002;3(3):279–98. doi:10.3970/cmes.2002.003.279.

Confalonieri F, Perego U. Simulation of fracture and delamination in layered shells due to blade cutting. Journal of the Serbian Society for Computational Mechanics 2017;11(2):139–51. doi:10.24874/jsscm.2017.11.02.12.

Costanzo F, Allen DH. A continuum thermodynamic analysis of cohesive zone models. International Journal of Engineering Science 1995;33(15):2197–219. doi:10.1016/0020-7225(95)00066-7.

Davidson BD, Zhao W. An accurate mixed-mode delamination failure criterion for laminated fibrous composites requiring limited experimental input. Journal of Composite Materials 2007;41(6):679–702. doi:10.1177/0021998306071031.

Del Piero G, Raous M. A unified model for adhesive interfaces with damage, viscosity, and friction. European Journal of Mechanics - A/Solids 2010;29(4):496–507. doi:10.1016/j.euromechsol.2010.02.004.

Dimitri R, Trullo M, De Lorenzis L, Zavarise G. Coupled cohesive zone models for mixed-mode fracture: A comparative study. Engineering Fracture Mechanics 2015;148:145–79. doi:10.1016/j.engfracmech.2015.09.029.

Dunn HM. Micromechanics of paperboard deformation. Master's thesis; Massachusetts institute of technology; Cambridge, USA; 2000.

Evans AG, Hutchinson JW. Effects of non-planarity on the mixed mode fracture resistance of bimaterial interfaces. Acta Metallurgica 1989;37(3):909–16. doi:10.1016/0001-6160(89)90017-5.

Gilormini P, Diani J. Some features of the ppr cohesive-zone model combined with a linear unloading/reloading relationship. Engineering Fracture Mechanics 2017;173(Supplement C):32 – 40. doi:10.1016/j.engfracmech.2017.01.017.

Gong Y, Zhao L, Zhang J, Hu N. An improved power law criterion for the delamination propagation with the effect of large-scale fiber bridging in composite multidirectional laminates. Composite Structures 2018;184:961–8. doi:10.1016/j.compstruct.2017.10.076.

Greenhalgh ES. Failure Analysis and Fractography of Polymer Composites. Woodhead Publishing Limited, 2009.

Guiamatsia I, Nguyen GD. A thermodynamics-based cohesive model for interface debonding and friction. International Journal of Solids and Structures 2014;51(3-4):647–59. doi:10.1016/j.ijsolstr.2013.10.032.

Högberg JL. Mixed mode cohesive law. International Journal of Fracture 2006;141(3-4):549–59. doi:10.1007/s10704-006-9014-9.

Hu N, Zemba Y, Okabe T, Yan C, Fukunaga H, Elmarakbi AM. A new cohesive model for simulating delamination propagation in composite laminates under transverse loads. Mechanics of Materials 2008;40(11):920–35. doi:10.1016/j.mechmat.2008.05.003.

Hutchinson JW, Suo Z. Mixed Mode Cracking in Layered Materials; Elsevier; volume 29 of *Advances in Applied Mechanics*. p. 63–191. doi:10.1016/s0065-2156(08)70164-9.

Jiang WG, Hallett SR, Green BG, Wisnom MR. A concise interface constitutive law for analysis of delamination and splitting in composite materials and its application to scaled notched tensile specimens. International Journal for Numerical Methods in Engineering 2007;69(9):1982–95. doi:10.1002/nme.1842.

Krueger R. Development and application of benchmark examples for Mixed-Mode I/II Quasi-Static delamination propagation predictions. NASA Technical Reports 2012;NASA/CR-2012-217562(April):1–57. URL:

http://ntrs.nasa.gov/search.jsp?R=20120007197.

Lee S. Mode II delamination failure mechanisms of polymer matrix composites. Journal of Materials Science 1997;32(5):1287–95. doi:10.1023/a:1018552506085.

Lemaitre J, Chaboche J. Mechanics of Solid Materials. Cambridge University Press, 1994.

Leuschner M, Fritzen F, van Dommelen JAW, Hoefnagels JPM. Potential-based constitutive models for cohesive interfaces: Theory, implementation and examples. Composites Part B: Engineering 2015;68:38–50. doi:10.1016/j.compositesb.2014.08.024.

Li Y, Reese S, Simon JW. Modeling the fiber bridging effect in cracked wood and paperboard using a cohesive zone model. Engineering Fracture Mechanics 2018;196:83–97. doi:10.1016/j.engfracmech.2018.04.002.

Lofti HR, Shing PB. Interface model applied to fracture of masonry structures. ASCE Journal of Structural Engineering 1994;120(1):63–80. doi:10.1061/(ASCE)0733-9445(1994)120:1(63).

Mosler J, Scheider I. A thermodynamically and variationally consistent class of damage-type cohesive models. Journal of the Mechanics and Physics of Solids 2011;59(8):1647–68. doi:10.1016/j.jmps.2011.04.012.

de Moura MFSF, Gonçalves JPM, Silva FGA. A new energy based mixed-mode cohesive zone model. International Journal of Solids and Structures 2016;102-103:112–9. doi:10.1016/j.ijsolstr.2016.10.012.

Nguyen N, Waas AM. A novel mixed-mode cohesive formulation for crack growth analysis. Composite Structures 2016;156:253–62. doi:10.1016/j.compstruct.2015.11.015.

Ortiz M, Pandolfi A. Finite-deformation irreversible cohesive elements for three-dimensional crack-propagation analysis. International Journal for Numerical Methods in Engineering 1999;44(9):1267–82. doi:10.1002/(sici)1097-0207(19990330)44:9<1267::aid-nme486>3.0.co;2-7.

Ottosen NS, Ristinmaa M. Thermodynamically based fictitious crack/interface model for general normal and shear loading. International Journal of Solids and Structures 2013;50(22-23):3555–61. doi:10.1016/j.ijsolstr.2013.06.019.

Park K, Paulino GH. Cohesive zone models: A critical review of Traction-Separation relationships across fracture surfaces. Applied Mechanics Reviews 2013;64(6):060802. doi:10.1115/1.4023110.

Park K, Paulino GH, Roesler JR. A unified potential-based cohesive model of mixed-mode fracture. Journal of the Mechanics and Physics of Solids 2009;57(6):891–908. doi:10.1016/j.jmps.2008.10.003.

Parrinello F, Marannano G, Borino G. A thermodynamically consistent cohesive-frictional interface model for mixed mode delamination. Engineering Fracture Mechanics 2016;153:61–79. doi:10.1016/j.engfracmech.2015.12.001.

Pinho S. Modelling failure of laminated composites using physically-based failure models. Ph.D. thesis; Imperial College, London; 2005.

Pinho S, Iannucci L, Robinson P. Formulation and implementation of decohesion elements in an explicit finite element code. Composites Part A: Applied Science and Manufacturing 2006;37:778–89. doi:10.1016/j.compositesa.2005.06.007.

Raous M, Cangémi L, Cocua M. A consistent model coupling adhesion, friction, and unilateral contact. Computer Methods in Applied Mechanics and Engineering 1999;177(3-4):383–99. doi:10.1016/S0045-7825(98)00389-2.

Reeder JR. An evaluation of mixed-mode delamination failure criteria. NASA Technical Reports 1992;104210(February):1–50. URL: https://ntrs.nasa.gov/search.jsp?R=19920009705.

Reeder JR, Crews JH. Mixed-mode bending method for delamination testing. AIAA Journal 1990;28(7):1270–6. doi:10.2514/3.25204.

Serpieri R, Sacco E, Alfano G. A thermodynamically consistent derivation of a frictional-damage cohesive-zone model with different mode I and mode II fracture energies. European Journal of Mechanics - A/Solids 2015;49:13–25. doi:10.1016/j.euromechsol.2014.06.006.

Simon JW, Höwer D, Stier B, Reese S, Fish J. A regularized orthotropic continuum damage model for layered composites:

intralaminar damage progression and delamination. Computational Mechanics 2017;60(3):445–63. doi:10.1007/s00466-017-1416-1.

Spring DW, Giraldo-Londono O, Paulino GH. A study on the thermodynamic consistency of the Park–Paulino–Roesler (PPR) cohesive fracture model. Mechanics Research Communications 2016;78, Part B:100 –9. doi:10.1016/j.mechrescom.2016.05.006.

Spring DW, Paulino GH. Computational homogenization of the debonding of particle reinforced composites: The role of interphases in interfaces. Computational Materials Science 2015;109:209–24. doi:10.1016/j.commatsci.2015.07.012.

Swentek I, Wood JT. Measuring polymer composite interfacial strength. Composites Part B: Engineering 2014;58:235–41. doi:10.1016/j.compositesb.2013.10.069.

Turon A, Camanho PP, Costa J, Dávila CG. A damage model for the simulation of delamination in advanced composites under variable-mode loading. Mechanics of Materials 2006;38(11):1072–89. doi:10.1016/j.mechmat.2005.10.003.

Valoroso N, Champaney L. A damage-mechanics-based approach for modelling decohesion in adhesively bonded assemblies. Engineering Fracture Mechanics 2006;73(18):2774–801. doi:10.1016/j.engfracmech.2006.04.029.

Xia Q, Boyce MC, Parks DM. A constitutive model for the anisotropic elasticplastic deformation of paper and paperboard. International Journal of Solids and Structures 2002;39(15):4053–71. doi:10.1016/s0020-7683(02)00238-x.

Yuan Z, Fish J. Are the cohesive zone models necessary for delamination analysis? Computer Methods in Applied Mechanics and Engineering 2016;310:567–604. doi:10.1016/j.cma.2016.06.023.